

Supplementary Material for:

**Efficient radioactive gas detection
by porous metal-organic framework scintillating nanocrystals.**

M. Orfano¹, J. Perego¹, F. Cova¹, C. X. Bezuidenhout¹, S. Piva¹, C. Dujardin², B. Sabot³, S. Pierre³,
P. Mai², C. Daniel⁴, S. Bracco¹, A. Vedda^{1*}, A. Comotti^{1,*}, A. Monguzzi^{1,*}

¹ *Dipartimento di Scienza dei Materiali, Università degli Studi Milano-Bicocca, Milano – ITALY*

² *Institut Lumière Matière, Université Claude Bernard Lyon 1, Lyon – France*

³ *Université Paris-Saclay, CEA, LIST, Laboratoire National Henri Becquerel (LNE-LNHB), F-91120 Palaiseau – France*

⁴ *Nano Active Film SRL, Dipartimento di Chimica e Biologia, Università degli Studi di Salerno, Fisciano (SA) - Italy*

E-mail: anna.vedda@unimib.it - angiolina.comotti@unimib.it - angelo.monguzzi@unimib.it

INDEX

1. SYNTHESIS	page 3
2. EXPERIMENTAL AND COMPUTATIONAL METHODS	page 6
3. Hf-DPA-x: MODULATION OF CRYSTAL SIZE AND SHAPE	page 10
3.1. Powder X-ray diffraction of Hf-DPA-x	
3.2. FT-IR spectra of Hf-DPA-x	
3.3. SEM images of Hf-DPA-x	
4. REPRODUCIBILITY OF Hf-DPA SYNTHESIS	page 13
4.1. Powder X-ray diffraction of Hf-DPA	
4.2. Gas adsorption analysis	
5. Hf-DPA	page 16
5.1. SEM images and EDS analysis	
5.2. Powder X-ray diffraction and structure refinement	
5.3. Thermogravimetric analysis	
5.4. Infrared spectroscopy	
5.5. ¹H liquid NMR of digested Hf-DPA	
5.6. Solid state NMR	
5.7. Gas adsorption analysis	
6. TIME RESOLVED PHOTOLUMINESCENCE DATA ANALYSIS	page 33
7. PHOTOLUMINESCENCE QUANTUM YIELD MEASUREMENTS	page 33
8. TEMPERATURE DEPENDENT SPECTROSCOPY	page 34
9. COMPARATIVE RADIOLUMINESCENCE EXPERIMENTS	page 35
10. GRAND CANONICAL MONTE CARLO (GCMC) GAS ADSORPTION SIMULATIONS	page 36
11. TRIPLE TO DOUBLE COINCIDENCE TECHNIQUE	page 41
12. GAS DETECTION DATA REPRODUCIBILITY	page 44
13. SUPPLEMENTARY REFERENCE	page 44

1. SYNTHESIS

9,10-dibromoanthracene (95%) and 4-(methoxycarbonyl)phenylboronic acid (97%) were purchased from Fluorochem. Pd(PPh₃)₂Cl₂, hafnium tetrachloride (HfCl₄, 98%), potassium carbonate, potassium hydroxide, acetonitrile, ethanol (EtOH), tetrahydrofuran (THF), formic acid, dry dimethylformamide (DMF) and chloroform (CHCl₃) were purchased from Merck.

Synthesis of 9,10-bis(4-carboxyphenyl)anthracene ligand

9,10-bis(4-carboxyphenyl)anthracene (DPA) was synthesized using a Suzuki coupling with a modified procedure.^{1,2}

Briefly, 9,10-dibromoanthracene (1 g, 2.98 mmol) and 4-(methoxycarbonyl)phenylboronic acid (1.18 g, 6.55 mmol) were dispersed in a 1:1 acetonitrile/water mixture (20 mL each) in a Schlenk tube. Nitrogen was bubbled for 1 hour to remove the oxygen from the reaction vessel. Potassium carbonate (2.89 g, 20.9 mmol) and Pd(PPh₃)₂Cl₂ (0.25 g, 0.36 mmol) were added and the reaction was stirred and heated at 100°C for 96 hours. The reaction was allowed to cool to room temperature and rotary dried under vacuum. The product was extracted with chloroform, dried over anhydrous sodium sulphate, filtered and rotary dried under vacuum. The yellow solid was purified by column chromatography using chloroform as eluent. A yellowish crystalline solid was recovered after rotary evaporation and was dried under high vacuum to obtain dimethyl 4,4'-(anthracene-9,10-diyl)dibenzoate. Yield: 1.25 g, 51.3 %. ¹H-NMR (400 MHz, CDCl₃): δ (ppm) = 4.03 ppm (6H, s), 7.35 ppm (4H, m), 7.58 ppm (4H, d), 7.63 ppm (4H, m), 8.30 ppm (4H, d). The spectrum was calibrated using residual solvent peaks (CHCl₃ at δ = 7.26 ppm) as internal standards.

Then, the yellow solid (1g, 2.24 mmol) was dispersed in a mixture of THF (90 mL), ethanol (30 mL) and deionized water (30 mL) and potassium hydroxide (1.56 g, 27.8 mmol) was added. The mixture was stirred and heated at 66°C for 24 hours. The completion of the reaction was assessed by TLC analysis using chloroform as eluent. Then, the mixture was allowed to cool to room temperature and concentrated HCl was added until pH ~ 1. The organic solvent was removed by rotary evaporation and the precipitate was collected by filtration and washed with deionized water. The solid was dried under vacuum and recrystallized from THF to obtain 9,10-bis(4-carboxyphenyl)anthracene. Yield: 0.65 g; 70 %. ¹H-NMR (400 MHz, DMSO-d₆): δ (ppm) = 7.45 ppm (4H, m), 7.55 ppm (4H, m), 7.62 ppm (4H, d), 8.23 ppm (4H, m). The spectrum was calibrated using residual solvent peaks (DMSO at δ = 2.50 ppm) as internal standards.

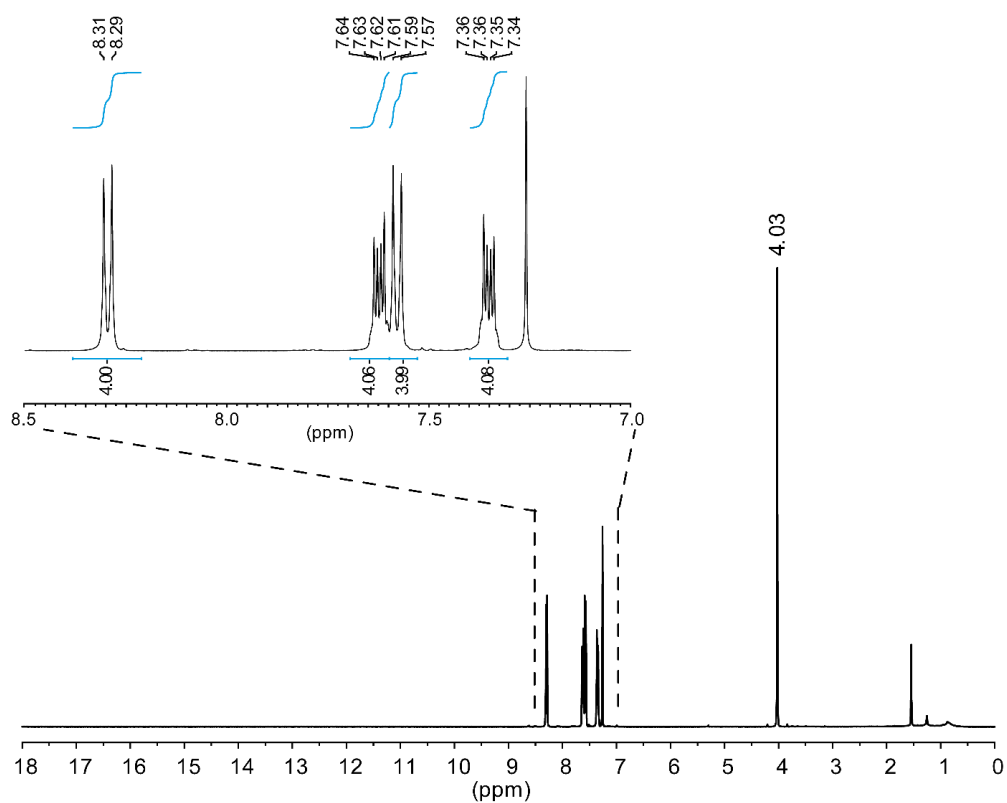


Figure S1 | ^1H liquid NMR of dimethyl 4,4'-(anthracene-9,10-diyl)dibenzoate. The spectrum was collected on a AVANCE NEO Bruker instrument (400 MHz) at 298.1 K in CDCl_3 .

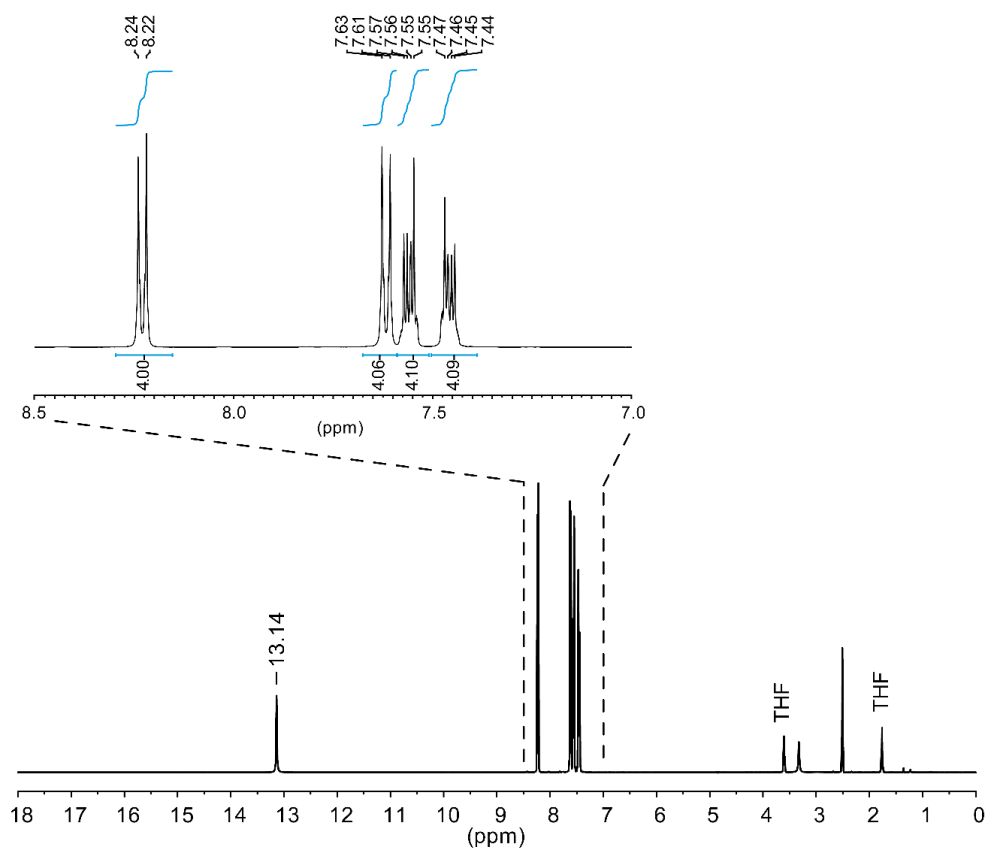


Figure S2 | ^1H liquid NMR of 9,10-bis(4-carboxyphenyl)anthracene. The spectrum was collected on a AVANCE NEO Bruker instrument (400 MHz) at 298.1 K in DMSO_d_6 .

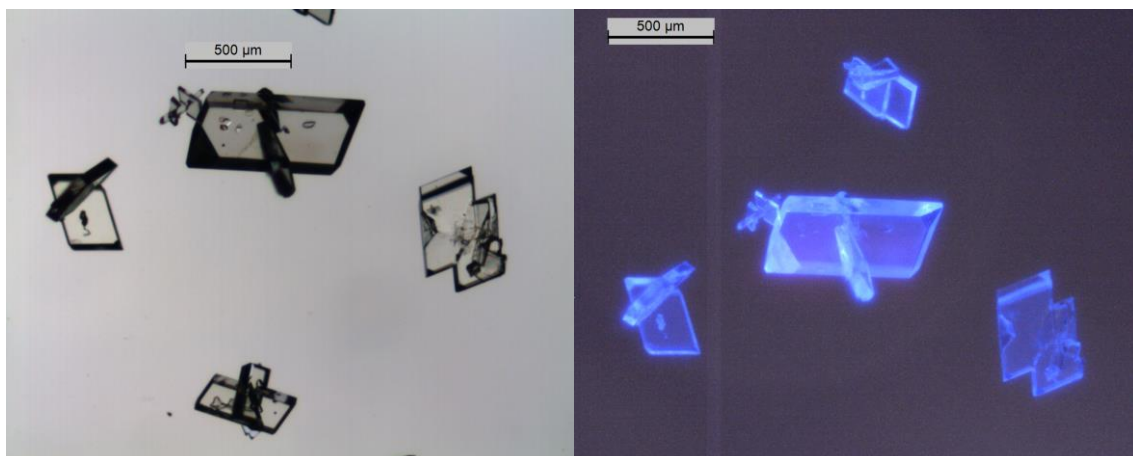


Figure S3 | Optical microscopy images of crystals of 9,10-bis(4-carboxyphenyl)anthracene under sunlight (left) and under UV light (365 nm, right).

Synthesis of Hf-DPA-x MOFs

MOF crystal growth was controlled by an increasing amount of modulator (formic acid). The screening reaction was performed on a small scale of tens of milligram.

9,10-bis(4-carboxyphenyl)anthracene (10.44 mg; 0.025 mmol) and HfCl₄ (8.0 mg; 0.025 mmol) were added to a 12 mL glass vials. Dry DMF (2.5 mL) and the proper amount of formic acid (see Table 1) was added. The mixture was sonicated for 60 seconds to produce a homogeneous dispersion and the vials were heated in a preheated oven at 120 °C for 22 hours. Then, the vials were removed from the oven and cooled down to RT. The yellowish solid was filtered on a 0.2 μm PTFE membrane and washed with DMF (3 x 10 mL) and then with CHCl₃ (3 x 10 mL). The powder was recovered and dried at 120 °C under high vacuum before further analysis.

Table 1. Formic acid used in Hf-DPA-x MOFs synthesis.

Sample	Formic acid (μL)
Hf-DPA-2	2
Hf-DPA-10	10
Hf-DPA-20	20
Hf-DPA-25	25
Hf-DPA-40	40
Hf-DPA-100	100
Hf-DPA-200	200
Hf-DPA-300	300
Hf-DPA-400	400

Scale-up synthesis of Hf-DPA

9,10-bis(4-carboxyphenyl)anthracene (209.0 mg; 0.5 mmol) and HfCl₄ (160.0 mg; 0.5 mmol) were added to a 100 mL pyrex bottle with cleavable teflon lined cap. Dry DMF (50 mL) and 400 μL of formic acid were added and the bottle was closed and sonicated for 60 seconds to obtain a well-dispersed mixture. The mixture was heated at 120 °C for 22 hours in a preheated oven. Then, the glass bottle was removed from the oven and cooled to RT. The yellowish solid was collected by filtration on a 0.2 μm PTFE membrane and washed with DMF (3 x 100 mL) and then CHCl₃ (3 x 100 mL). The powder was recovered and dried at 120 °C under high vacuum before further

analysis. Yield: 178 mg (58 %). The same synthesis was performed to produce the samples Hf-DPA, Hf-DPA-a, Hf-DPA-b and Hf-DPA-c to test the reproducibility of the procedure.

2. EXPERIMENTAL AND COMPUTATIONAL METHODS

Scanning electron microscopy (SEM) and energy-dispersive spectroscopic analysis (EDS). Scanning electron microscopy (SEM) images were collected using a Zeiss Gemini 500 microscope, operating at 5 KV and a working distance of 4.7 mm. The sample was deposited on a silicon slide from 2-propanol dispersion, dried under high vacuum and sputtered with gold before the analysis (10 nm, nominal thickness). Particle size distributions were measured from SEM images using ImageJ software. The linear dimensions of nanocrystals have been evaluated over more than 100 particles to determine the particle size distribution. Energy-dispersive spectroscopy (EDS) was performed using a Bruker XFlash 6-30 detector accessory. MOF nanocrystals were dispersed in 2-propanol and deposited on a graphite stab, dried under high vacuum, and coated with graphite before the analysis.

Gas adsorption properties. N₂ and Ar adsorption isotherms at 77 K were collected up to 1 bar using a Micromeritics analyzer ASAP2020 HD. Kr adsorption isotherms at 77 K and 298 K up to 1 bar were collected on a Micromeritics Triflex instrument. Samples were previously outgassed overnight at 130 °C under high vacuum (10⁻³ mmHg) to remove the adsorbed species. N₂, Ar and Kr adsorption isotherms at 77K were fitted using Langmuir and BET models and surface areas were calculated in the range from 0.015 to 0.08 p/p^o (radii of N₂ = 0.162 nm, Ar = 0.1940 nm and Kr = 0.207 nm).³ Pore size distributions (PSD) were calculated according to Non-Local Density Functional Theory (NLDFT) model.

Fourier transform infrared (FTIR) spectroscopy. FTIR spectra measurements were performed with a Jasco FT/IR 4100 equipped with an ATR PRO450-S module. MOFs samples were evacuated under high vacuum at 130°C before analysis to ensure the complete removal of adsorbed water vapor and guest species. Spectra were collected between 600 cm⁻¹ and 4000 cm⁻¹ with resolution of 2.0 cm⁻¹.

Nuclear magnetic resonance (NMR) spectroscopy. ¹H-NMR spectra were recorded on a AVANCE NEO Bruker instrument (400 MHz). MOFs samples were digested with deuterated trifluoroacetic acid (TFA-d, 0.1 mL) and the solution was diluted with deuterated dimethyl sulfoxide (DMSO-d₆, 1 mL).

Thermogravimetric analysis (TGA). TGA were performed using a Mettler Toledo Star System 1 equipped with a gas controller GC10. The experiments were conducted applying a ramp from 30°C to 1000°C and a scan rate of 10°C/min in dry air.

Powder X-ray diffraction. PXRD measurements of Hf-DPA-x were collected with a Rigaku Smartlab powder diffractometer over a range for 2θ of 3.0 – 50.0° with a step size of 0.02° and a scan speed of 1.0°·min⁻¹ using Cu-Kα radiation, 40 kV and 30 mA.

PXRD measurements of Hf-DPA, Hf-DPA-a, Hf-DPA-b, Hf-DPA-c were collected over a range for 2θ of 2.0 – 80.0° with a step size of 0.02° and a scan speed of 0.3°·min⁻¹ using Cu-Kα radiation, 40 kV, 30 mA. The activated powder samples were deposited on a zero-background silicon sample holder.

Synchrotron radiation PXRD experimental conditions. Samples were prepared and sealed in 0.5 mm Lindeman capillaries for XRD experiments at the ESRF ID22 beam line using a 0.354 Å wavelength. PXRD measurements were collected over a range of 0.0 – 32.0° with a data collection interval of 0.002° and data collection was done over 12 detectors simultaneously. The scan speed may vary depending on sample degradation. Data were collected on various spots along the capillary and multiple times on the same spot. Any scans which showed signs of degradation were excluded from the final merged and binned data set.

Solid state NMR. ¹³C and ¹H solid-state NMR experiments were carried out at 75.5 and 300.1 MHz, respectively, with a Bruker Avance 300 instrument operating at a static field of 7.04 T equipped with high-power amplifiers (1 kW) and a 4 mm double resonance MAS probe. ¹³C{¹H} ramped-amplitude Cross Polarization (CP) experiments⁴ were performed at 293 K at a spinning speed of 12.5 kHz using a recycle delay of 5 s and contact times of 2 and 0.05 ms. The 90° pulse for proton was 2.9 μs. Quantitative ¹³C{¹H}

Single-Pulse Excitation (SPE) experiments were run using a 90° pulse of 4.6 μ s and a recycle of 60 s. Crystalline polyethylene was taken as an external reference at 32.8 ppm from TMS.

Phase-modulated Lee–Goldburg (PMLG) heteronuclear ^1H - ^{13}C correlation (HETCOR) experiments coupled with fast magic angle spinning allowed the recording of the 2D spectra with a high resolution in both hydrogen and carbon dimensions.^{5,6} Narrow hydrogen resonances, with line widths on the order of 1–2 ppm, were obtained with homonuclear decoupling during t_1 ; this resolution permits a sufficiently accurate determination of the proton species in the system. The 2D ^1H - ^{13}C PMLG HETCOR spectra were run with an LG period of 18.9 μ s. The efficient transfer of magnetization to the carbon nuclei was performed by applying the RAMP-CP sequence. Quadrature detection in t_1 was achieved by the time proportional phase increments method (TPPI). The carbon signals were acquired during t_2 under proton decoupling by applying the two-pulse phase modulation scheme (TPPM).⁷ The 2D ^1H - ^{13}C PMLG HETCOR NMR spectra of Hf-DPA MOF were conducted at 298 K under magic-angle spinning (MAS) conditions at 12.5 kHz with contact times of 2 and 0.05 ms.

Hyperpolarization ^{129}Xe NMR experiments were performed by a home-built apparatus with a continuous-flow delivery of hyperpolarized xenon gas with a Bruker Avance 300 spectrometer operating at a Larmor Frequency of 83.02 MHz for ^{129}Xe . A diode array laser delivering 6 W at 795 nm was applied, circular polarization was achieved using a beam splitting cube and quarter wave plate. A stream of gas mixture containing 2% xenon, 2% nitrogen and 96% helium at 2 atm was used and the gas flow rate was maintained at 20 L/h. Hf-DPA MOF was activated at 130°C under high vacuum for 12 hours. A pulse duration of 7 μ s was applied, with a recycle delay of 0.5 s. Variable temperatures experiments in the range 293 - 188 K were achieved by flowing cooled nitrogen gas around the sample region. The ^{129}Xe NMR chemical shifts were referenced to xenon gas set at 0 ppm.

PW-DFT structural resolution and Rietveld Refinement. The Hf-DPA model for the Rietveld refinement was generated from our previously published Zr-DPA structure,⁸ replacing the Zirconium atoms with Hafnium. Rietveld structural refinements of the X-ray data were performed using the TOPAS-Academic64 V6 software package.⁹ For the final Rietveld refinement, the structure was modelled as a disordered system with a space group $Fm-3m$. The background was fitted and refined using a Chebyshev polynomial with 20 coefficients in the PXRD trace range from 0.5° to 20° 2theta with baseline shift refinement. The “Simple_Axial_Model” was used to account for the asymmetry in the peaks, especially at low 2-theta values, which are a result of the geometry of the XRD setup of the ID22 beamline at the ESRF. The peaks were fitted using a PearsonVII "PVII" function.

General Computational Details for Materials Studio Software Suite.¹⁰ The primitive unit-cell dimensions and all atomic coordinates were optimized as part of a periodic system in $P-1$ using the CASTEP module of the Materials Studio software suite. The optimizations were performed using the GGA PBE functional with Grimme’s DFT-D dispersion correction, and thresholds for geometry optimization and SCF convergence were chosen as 2×10^{-6} eV. For the Rietveld refinement, the structure was converted to a disordered system in the $Fm-3m$ space group while maintaining the molecular geometries. Single point energy calculations were performed using the GGA PBE functional, and threshold for SCF convergence were chosen as 1×10^{-6} eV. The calculated Milliken charges were applied to the model for molecular mechanics (MM) calculations.

Molecular Mechanics modified Dreiding ForceField.

Modified forcefield parameters for GCMC and MD simulations added to the Dreiding force field to describe the Hf-DPA MOF.

Type	Element symbol	description	van der Waals Form
H_	H	hydrogen	LJ 12 6
H__A	H	hydrogen, involved in hydrogen bonds	LJ 12 6
C_R	C	carbon, aromatic	LJ 12 6
Hf	Hf	Hafnium 4+	LJ 12 6
O31	O	oxygen, sp3, OH	LJ 12 6
O32	O	oxygen, sp3, OX	LJ 12 6
O_R	O	oxygen, aromatic	LJ 12 6

		Functional form	R ₀ (Å)	K ₀ (kcal/mol·Å ²)
Hf	O31	harmonic	2.253	1400
Hf	O32	harmonic	2.071	1400
Hf	O_R	harmonic	2.199	1400
O31	H__A	harmonic	0.972	700
O_R	C_R	harmonic	1.278	1050

			Functional form	K ₀ (kcal/mol·Å ²)	T ₀ (°)
Hf	O_31	Hf	harmonic	200	102.6
Hf	O_32	Hf	harmonic	200	116.8
Hf	O_R	C_R	harmonic	200	133
Hf	O_31	H__A	harmonic	100	115.8
O_31	Hf	O_31	harmonic	100	122.3
O_31	Hf	O_32	harmonic	100	70.1
O_32	Hf	O_32	harmonic	100	91.1
O_R	Hf	O_R	harmonic	100	79
O_R	C_R	O_R	harmonic	100	126.8
O_R	C_R	X	harmonic	100	116.585
X	C_R3	X	harmonic	120	120

			Functional form	T ₀ -1(°)	E-1(kcal/mol·Å ²)	T ₀ -2(°)	E-2 (kcal/mol·Å ²)
O_32	Hf	O_R	tablulated	82.9	100	142.4	100
O_31	Hf	O_R	tablulated	73.1	100	138.7	100

				Functional form	B (kcal/mol)	d	n
Hf	O_R	C_R	O_R	DIHEDRAL	2	2	1
					W ₀ (°)	K ₀ (kcal/mol)	
O_32	Hf	Hf	Hf	UMBRELLA	80	10.12	
O_31	Hf	Hf	Hf	UMBRELLA	80	25.99	

Pairwise Noble gas LJ parameters for GCMC and MD simulations added to the Dreiding force field.

Interaction	ϵ (kcal/mol)	σ (Å)
C-Ar	0.13265	3.79
O-Ar	0.157	3.61
H-Ar	0.06033	3.51
Ar-Ar	0.18567	3.3952
C-Kr	0.16106	3.91
O-Kr	0.17932	3.76
H-Kr	0.06623	3.69
Kr-Kr	0.25846	3.6274
C-Xe	0.1832	4.09
O-Xe	0.18799	3.97
H-Xe	0.06771	3.93
Xe-Xe	0.35951	3.949
C-Rn	0.20976	4.19
O-Rn	0.21013	4.1
H-Rn	0.07306	4.07
Rn-Rn	0.44512	4.15

The modified Dreiding forcefield parameters were validated against the available experimental adsorption for Ar and Kr.

Grand Canonical Monte Carlo simulations. GCMC simulations were performed using the cubic unit cell for Hf-DPA (32.79 Å × 32.79 Å × 32.79 Å) which contains 4 Octahedral and 8 tetrahedral spaces. We used our modified dreiding forcefield that were empirically adjusted to reproduce the experimental sorption data and adsorbed gas densities. Dispersion interactions cutoff were set at 12.5 Å and the simulations were performed using 10^6 production steps and 10^5 equilibration steps to ensure that the Monte Carlo has equilibrated at each step. GCMC simulations for Ar and Kr at 77 K for comparison to the experimental adsorption data. Then then Xe and Rn were calculated at 195 K since this xenon sorption cannot be performed at 77K (the pressure required is extremely low). Sorption simulations for all 4 noble gasses studied here were also performed at 298 K up to 1 bar. Fixed pressure GCMC calculation were performed at 5 kpa (0.05 bar) and 298 K to determine and visualize the density distribution of the 4 noble gasses within the cubic cell of Hf-DPA.

Krypton Diffusion Simulations. The optimized force-field used for the adsorption simulations were used for flexible MD simulations. Given how important lattice dynamics are on guest diffusion during MD simulations, our custom force field were also optimized for Zr-MOFs and Hf-MOFs. The metal-nodes were described according to the literature and modified to reproduce a stable metal cluster consistent with the PW-DFT optimized geometry. The C-X bond dynamics were described using the Dreiding force field, and the charges to the MOF atoms were calculated by the Hirshfeld charge method using PW-DFT calculations on the primitive unit cell. Nonbonded and bonded interactions among adsorbent atoms were modelled according to the Dreiding force field for everything except the noble gases. The nonbonding interactions for the noble gasses were described pairwise with all the other atomic species in the models. NPT MD simulations were performed using after optimizing the crystallographic unit cell using the Quasi-Newton to ensure a proper relaxed system prior to the MD simulations. The NHL thermostat was used with a 0.1 Q ratio and a 10ps Decay constant while the Andersen Barostat was used to simulate the external pressure with a cell time constant of 50 ps. (59) The simulation was run for 5n at 298 K to obtain equilibrated forces and velocities before the main simulation was performed for 15 ns.

3. Hf-DPA-x: MODULATION OF CRYSTAL SIZE AND SHAPE

Hf-based MOF containing DPA moieties were screened using different amount of modulator (formic acid). The reactions were conducted on a small scale (see SYNTHESIS). The amount of formic acid was varied between 2 and 400 μL , while all the other reaction parameters were kept fixed. The samples were denoted Hf-DPA-x (x = amount of formic acid). PXRD diffraction between 3° and 50° 2θ degree, FT-IR spectra and SEM images were collected for each sample to determine their structural and morphological properties.

3.1 Powder X-ray diffraction of Hf-DPA-x

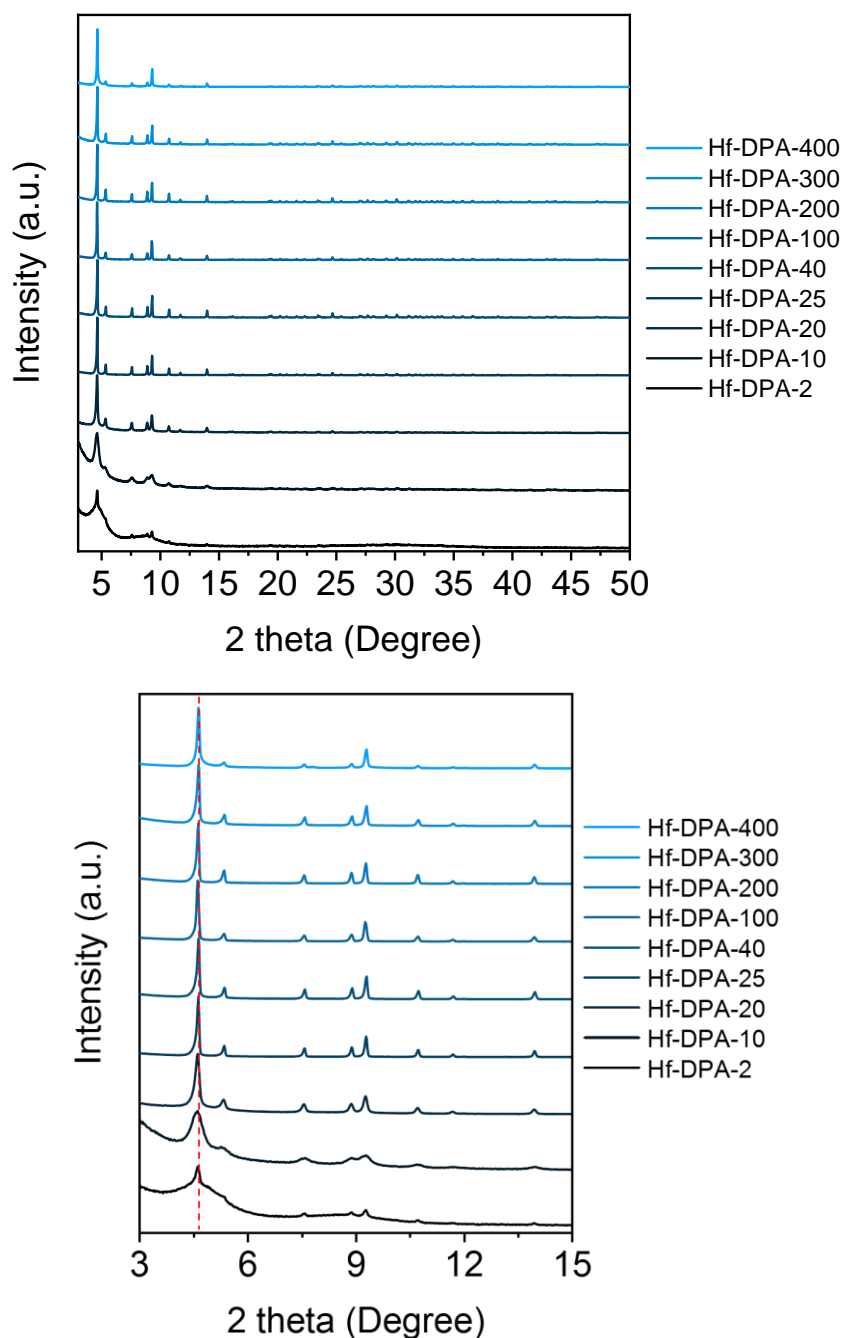


Figure S4 | Top: Powder X-ray diffraction patterns of samples Hf-DPA-x collected between 3° and 50° 2θ angle. Higher concentrations of formic acid $> 20 \mu\text{L}$ yield highly crystalline and phase pure materials. Sample Hf-DPA-2 and Hf-DPA-10, which were prepared with lower amount of formic acid ($< 20 \mu\text{L}$), display broad peaks due to small particle size and poor crystallinity. Bottom: enlargement between 3° and 15° 2θ angle.

3.2 FT-IR spectra of Hf-DPA-x

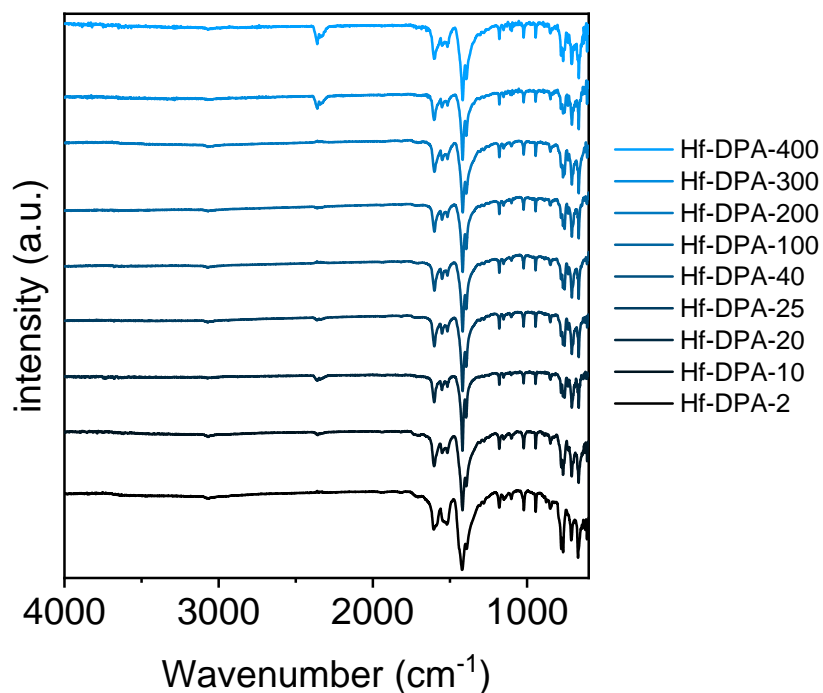


Figure S5 | FT-IR spectra of samples Hf-DPA-x collected between 4000 and 600 cm⁻¹.

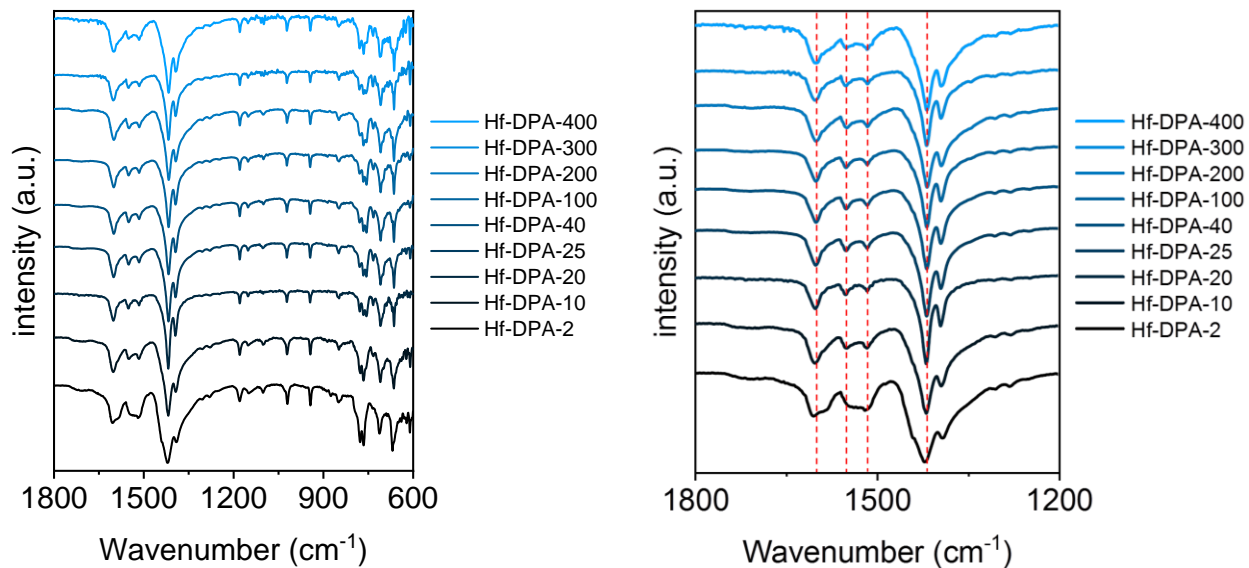


Figure S6 | FT-IR spectra of Hf-DPA-x collected between 1800 and 600 cm⁻¹ (left) and between 1800 and 1200 cm⁻¹ (right).

3.3 SEM images of Hf-DPA-x

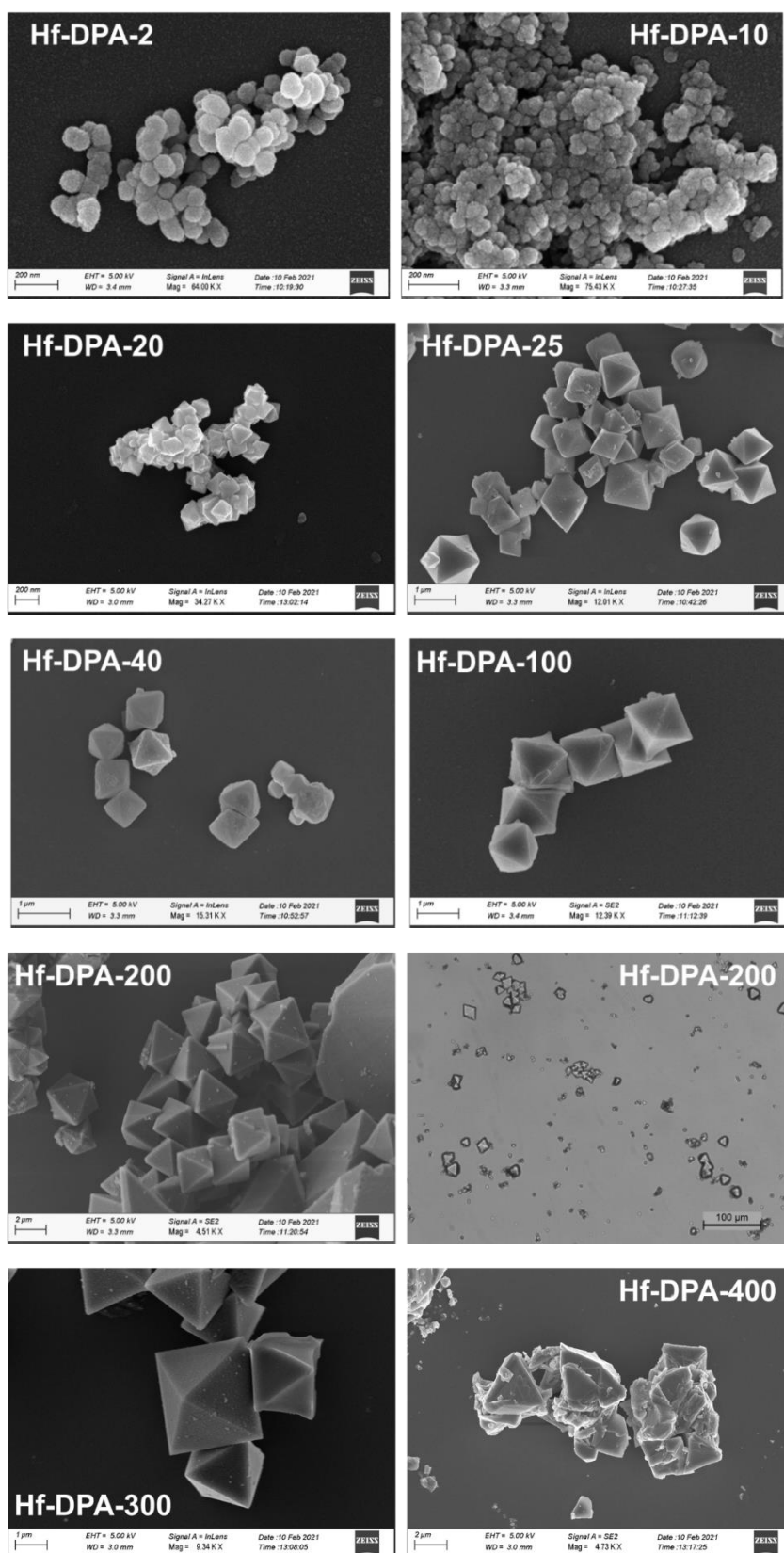


Figure S7 | SEM images of samples Hf-DPA-x and optical image of Hf-DPA-200. Sample Hf-DPA-2 and Hf-DPA-10 display spherical morphology. From sample Hf-DPA-20 to Hf-DPA-300, nanocrystalline samples with well-defined octahedral morphology can be obtained. Sample Hf-DPA-200 shows crystals of about 10-20 μm under optical microscope. Amount of modulator of 400 μL (Hf-DPA-400) produce broken and fractured crystals.

4. REPRODUCIBILITY OF Hf-DPA SYNTHESIS

4.1 Powder X-ray diffraction of Hf-DPA

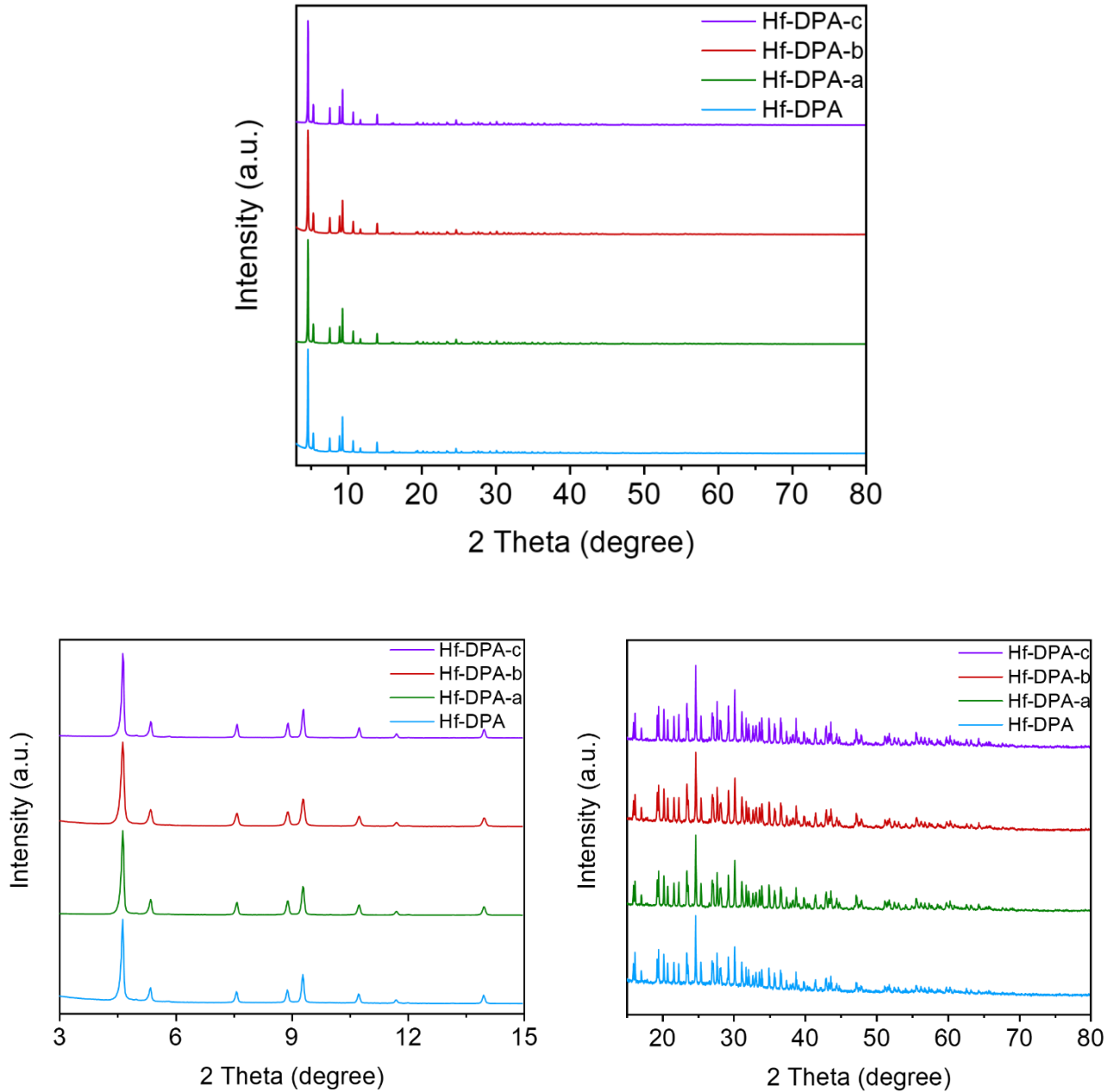


Figure S8 | Top: Powder x-ray diffraction patterns of Hf-DPA (light blue), Hf-DPA-a (green), Hf-DPA-b (red) and Hf-DPA-c (purple) collected on a Rigaku Smartlab diffractometer using Cu K_{α} radiation. Bottom, left: enlargement between 3° and 15° 2θ angle. Bottom, right: enlargement between 15° and 80° 2θ angle.

4.2 Gas adsorption analysis

N₂ adsorption isotherms at 77 K were collected for 4 different batches to test the reproducibility of sorption properties.

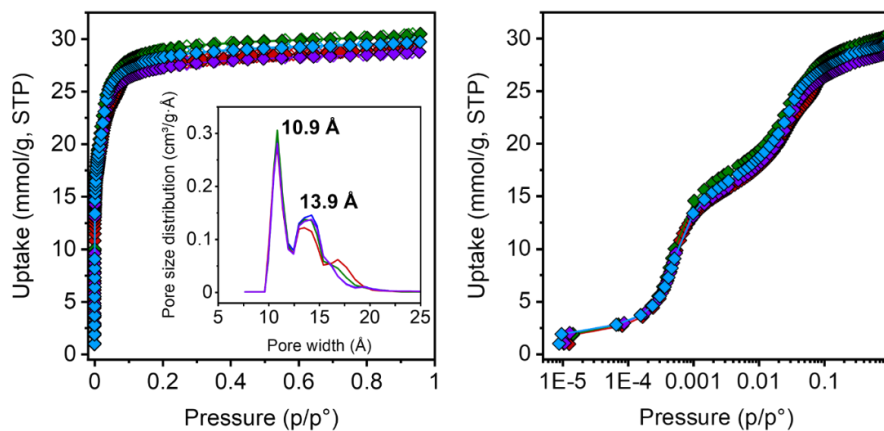


Figure S9 | N₂ adsorption isotherms collected at 77 K for 4 different batches of Hf-based MOF with the x-axis displayed in linear (left) and logarithmic scales (right). Inset: comparison of the differential pore size distributions calculated from the adsorption isotherms using NLDFT theory and carbon slit pore model. Hf-DPA (light blue), Hf-DPA-a (green), Hf-DPA-b (red) and Hf-DPA-c (purple).

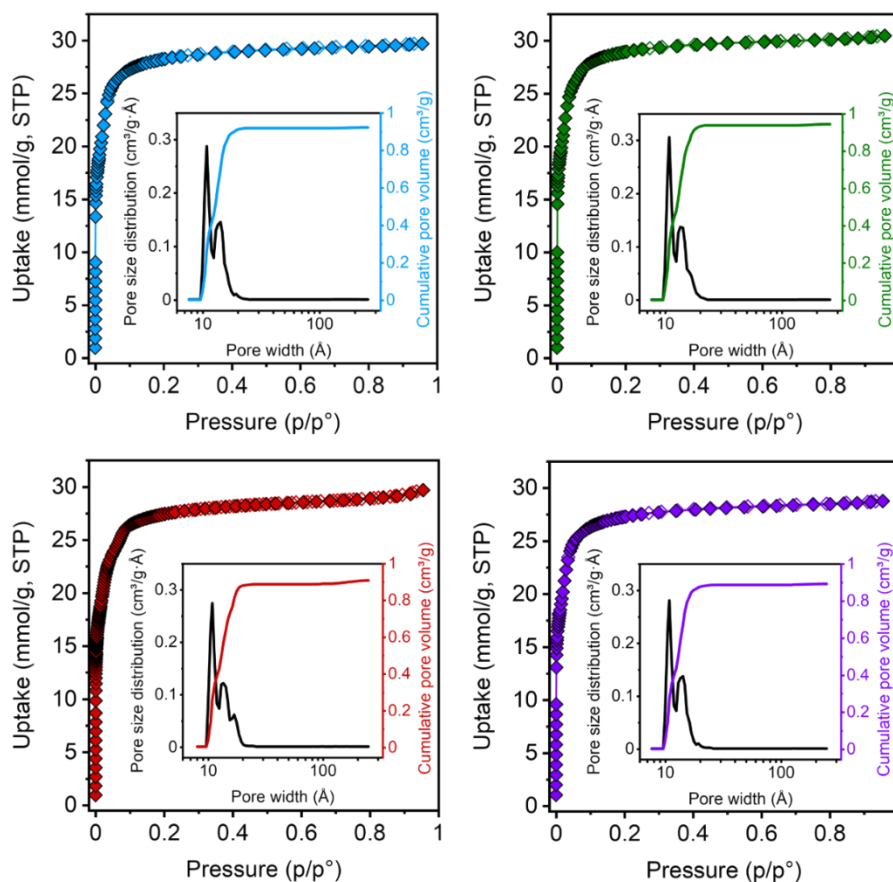


Figure S10 | N₂ adsorption isotherms of Hf-DPA (light blue), HfDPA-a (green), HfDPA-b (red) and HfDPA-c (purple). Insets: Differential pore size distributions and cumulative pore volume calculated from the adsorption isotherms using NLDFT theory and carbon slit pore model. Hf-DPA (light blue), Hf-DPA-a (green), Hf-DPA-b (red) and Hf-DPA-c (purple).

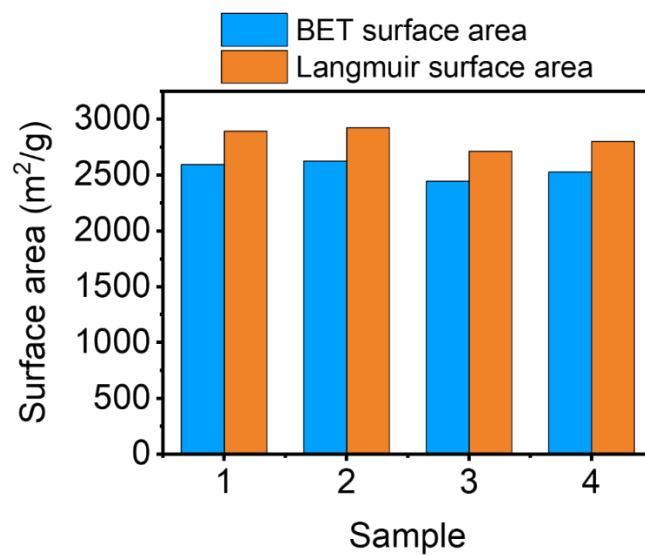


Figure S11 | BET and Langmuir surface areas of 4 different batches of Hf-based MOF. The mean surface area is $2550 \pm 70 \text{ m}^2/\text{g}$ and $2830 \pm 82 \text{ m}^2/\text{g}$ according to the BET and Langmuir models, respectively.

5. Hf-DPA

5.1 SEM images and EDS analysis

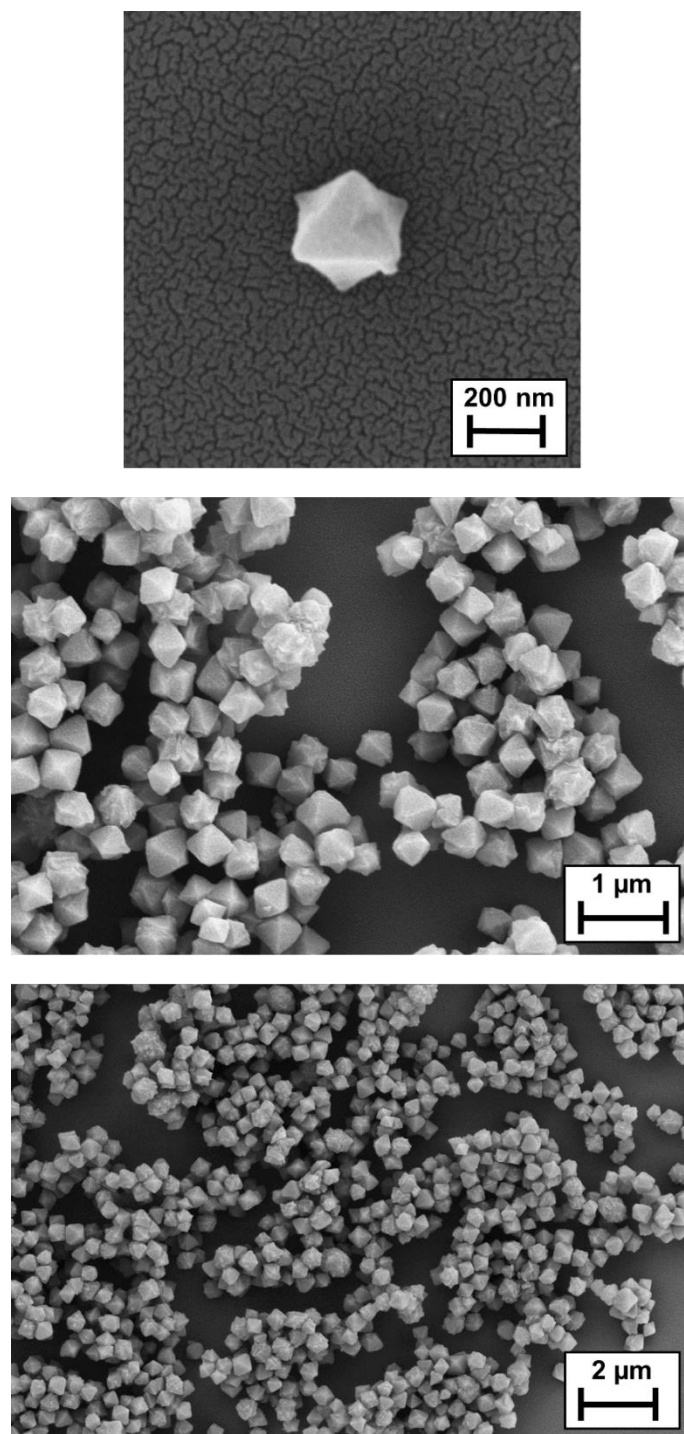


Figure S12 | Scanning electron microscopy (SEM) images of Hf-DPA at different magnification. Hf-MOF nanocrystals were casted on silicon surface and sputtered with gold before image acquisition.

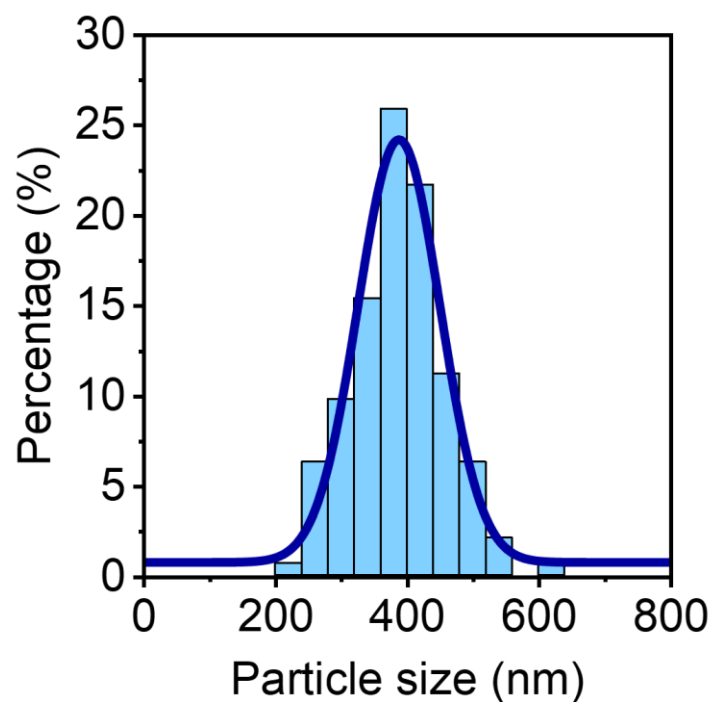


Figure S13 | Particle size distribution of Hf-DPA nanocrystals calculated from SEM images. The particle size was evaluated using more than 200 particles with software ImageJ. The data were fitted with a gaussian distribution (blue line).¹¹

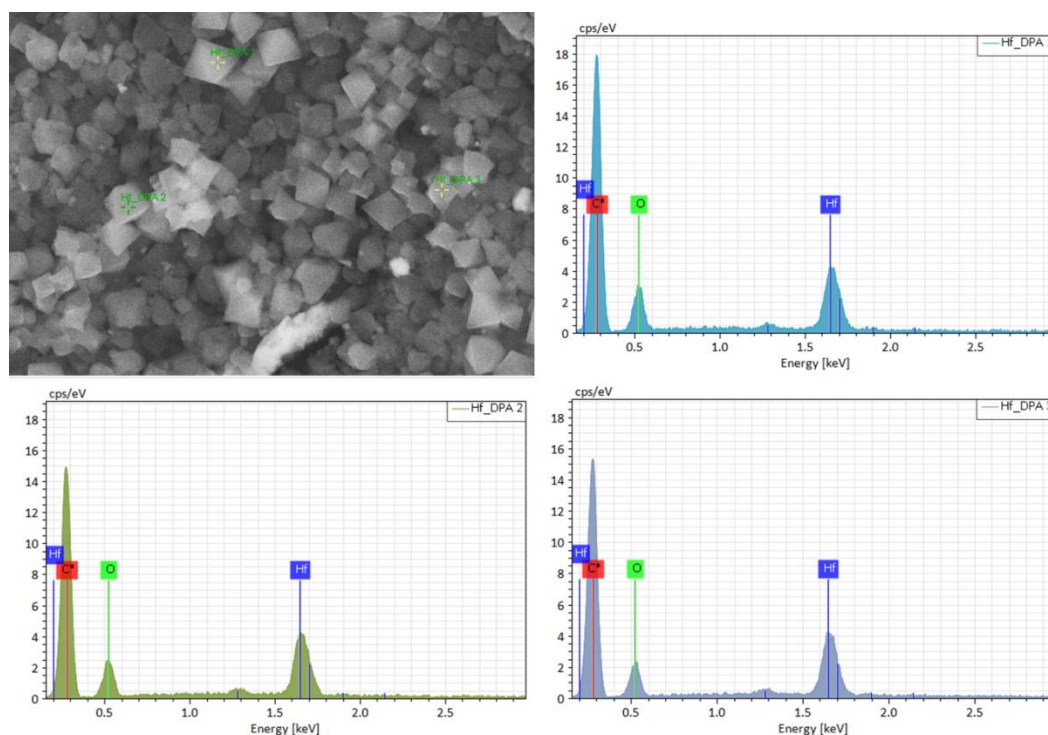


Figure S14 | EDS compositional analysis of Hf-DPA. The sample was deposited on a graphite stab and coated with graphite to increase the conductivity before EDS analysis.

5.2 Powder X-ray diffraction and structure refinement

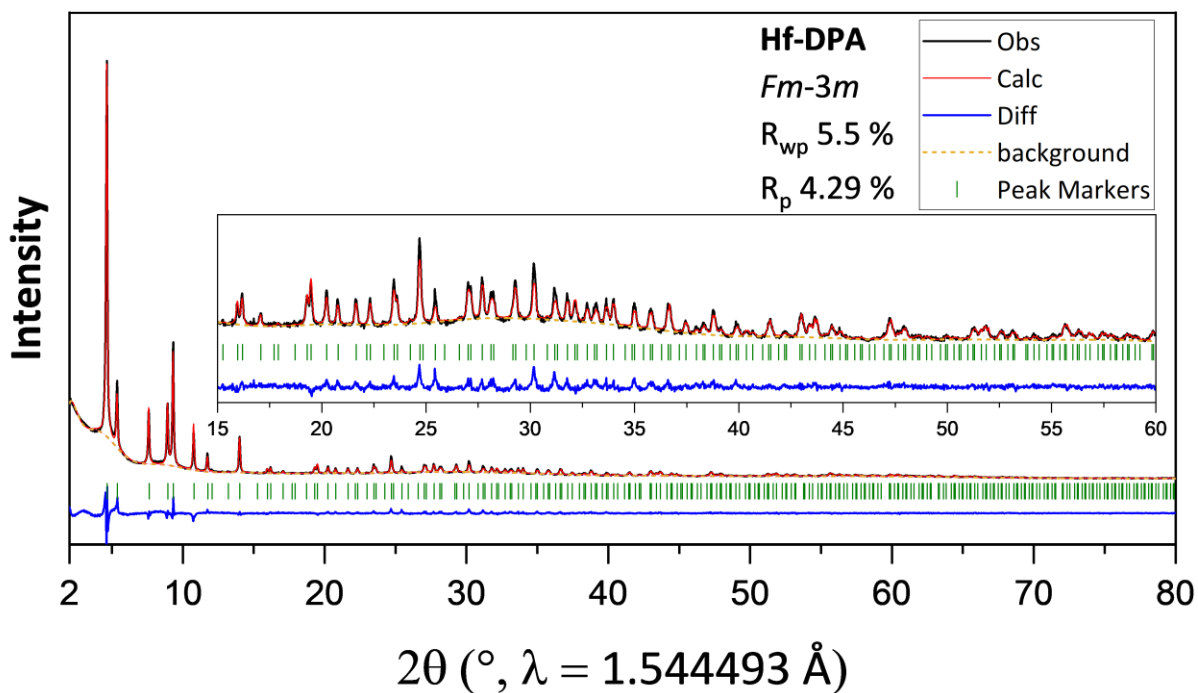


Figure S15 | The Rietveld refinement plot of PXRd pattern of activated Hf-DPA collected at RT. Data were collected with a Rigaku powder diffractometer using Cu-K α radiation.

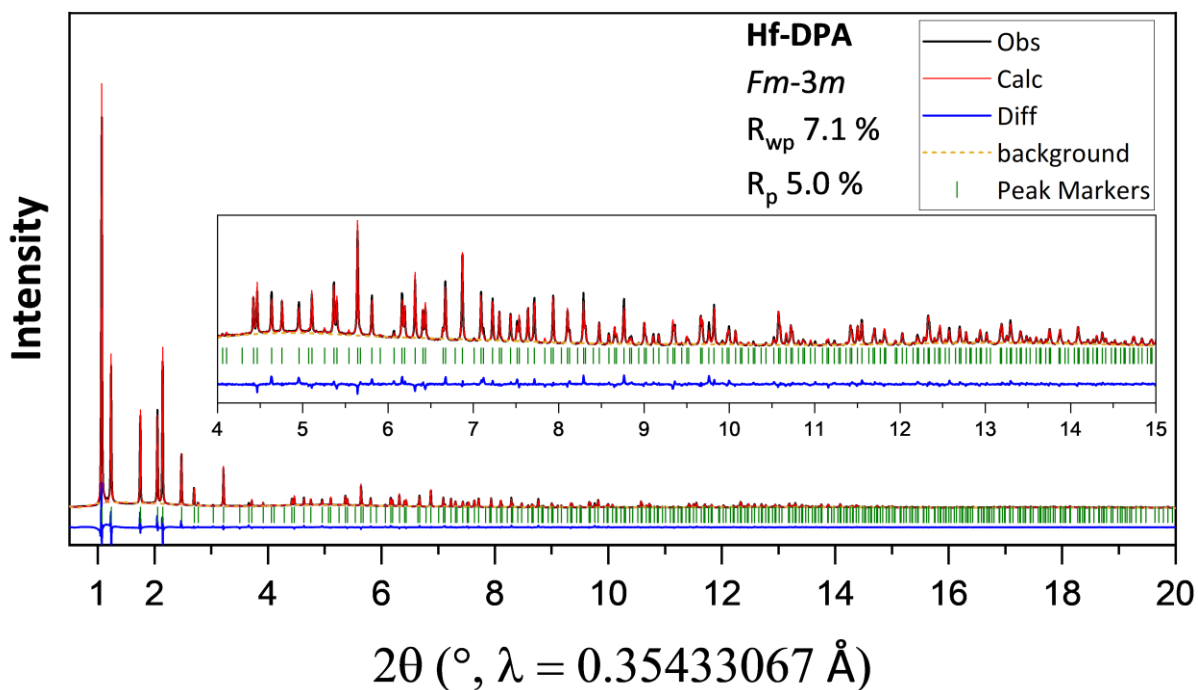


Figure S16 | The Rietveld refinement plot of synchrotron-source PXRd pattern of activated Hf-DPA collected at RT. Data were collected at the ESRF ID22 beamline by synchrotron radiation at 0.35433 \AA .

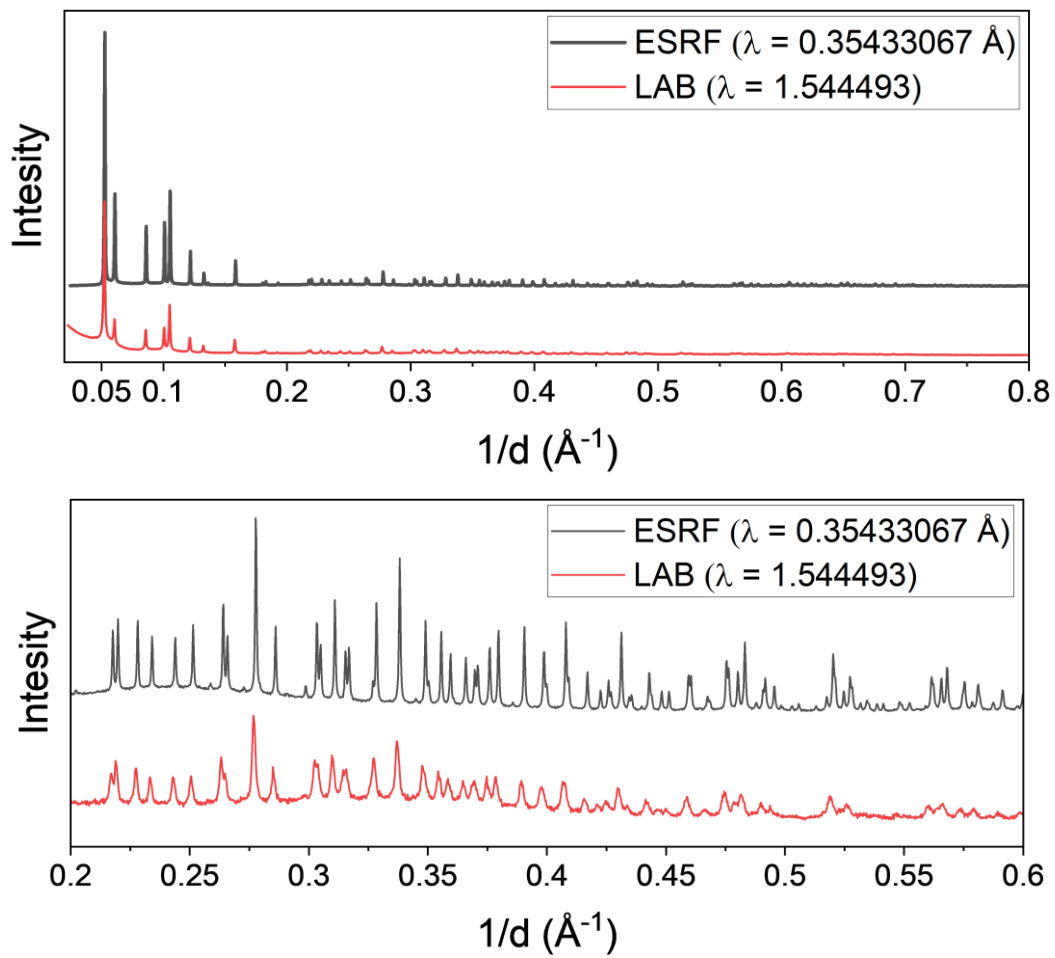


Figure S17 | Comparison of synchrotron-source PXRD and laboratory instrument PXRD data for Hf-DPA collected at RT.

Table 2. The refinement details and unit cell parameters for the Rietveld refinement of Hf-DPA performed at ambient temperature of PXRD data collected at the ESRF ID22 beamline using synchrotron radiation and using the Rigaku SmartLab instrument.

	Hf-DPA·xH ₂ O	Hf-DPA
Measurement device type	ESRF Synchrotron	SmartLab Rigaku
chemical formula (ASU)	C168 H100 O32 Hf6 · 70(H ₂ O)	C168 H100 O32 Hf6
formula weight (g/mol)	4823.39	3561.59
Z	4	4
Temp	RT	RT
Space group	<i>Fm-3m</i>	<i>Fm-3m</i>
$a = b = c$ (Å)	32.7916(2)	32.809(3)
V (Å ³)	35260.6(7)	35317(9)
ρ (g/cm ³)	0.910(3)	0.6961(2)
ρ (g/cm ³) without guest	0.697(3)	0.6961(2)
Rp (%)	5.0	4.3
Rwp (%)	7.1	5.5
Rbragg (%)	2.1	2.5
Refinement_method	Rietveld	Rietveld
measurement_type	Powder diffraction	Powder diffraction
measurement_device_type	ESRF Synchrotron	SmartLab Rigaku
radiation_wavelength (Å)	0.35433067	1.544493
measurement_method	CONTINUOUS SCAN	CONTINUOUS SCAN

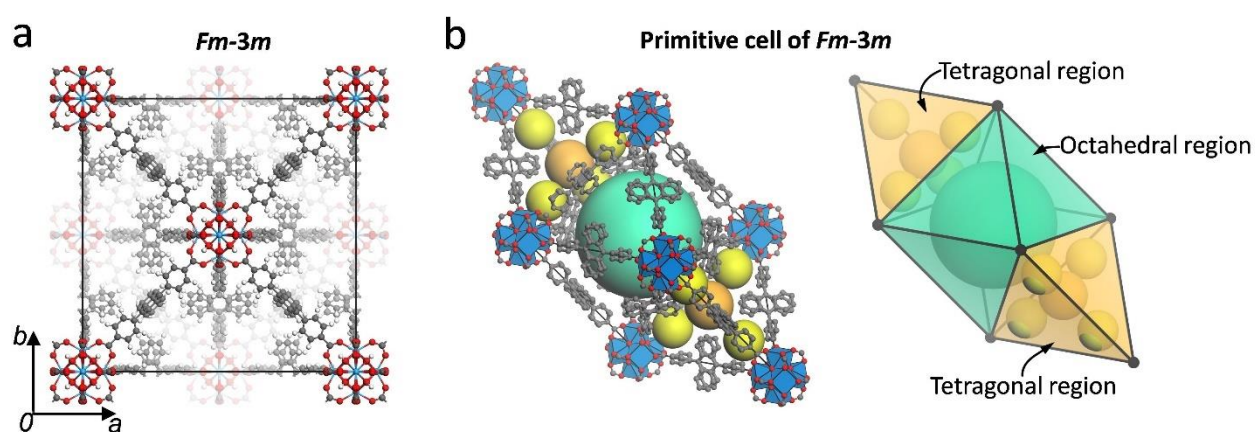


Figure S18 | a) The structure of Hf-DPA in the *Fm-3m* space group as refined from powder-XRD data. b-left) The primitive cell representation of the Hf-DPA structure with best fitted spheres included in the structure to highlight the void volumes. b-right) Representation of the connectivity between the nodes to highlight the tetragonal and octahedral regions.

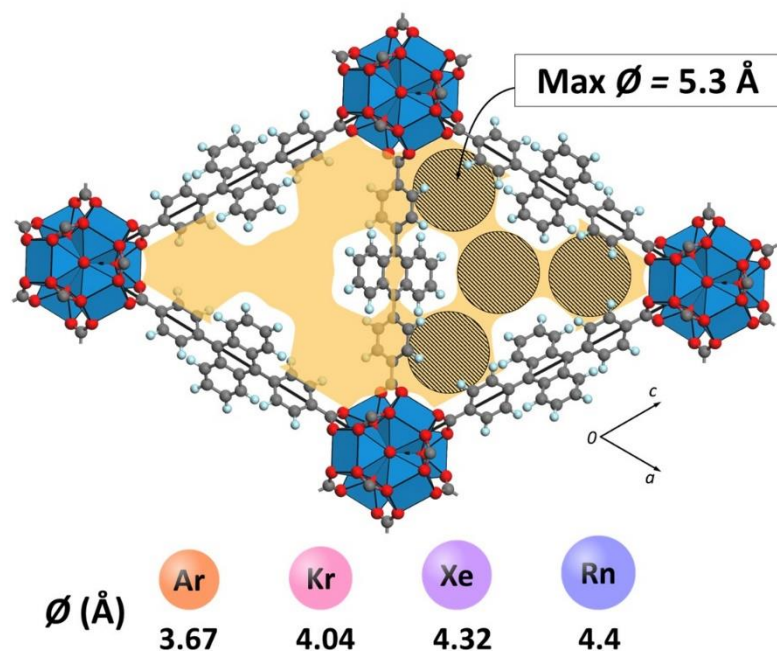


Figure S19 | Cross-sectional area in yellow of the Hf-DPA triangular windows as mapped using a probe radius of 1.2 Å. The grey circles indicate the maximum sphere diameter that can pass through the cross-section. Van der Waals diameters of the noble gases from Argon to Radon are shown below. {Haynes, 2016 #197} The radii of gas molecules are compatible with the pore size and can diffuse through the Hf-DPA structure unimpededly.

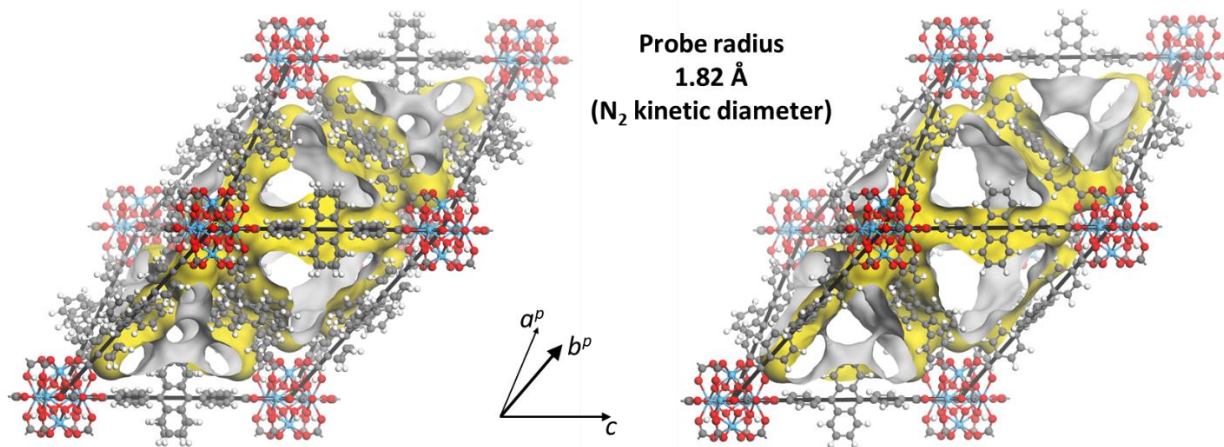


Figure S20 | Contact surface volumes calculated with a probe radius of 1.82 Å (shown in yellow, N₂ kinetic diameter is 3.64 Å and solvent radius of 1.82 Å) and a grid spacing of 0.4 Å.

Table 3. The pore volumes and surface areas determined using a probe radius of 1.82 Å for **Hf-DPA**. The sphere diameters equivalent to those of V_{oct} and V_{tet} are indicated.

Identification code	Hf-DPA	
	Disordered model	Ordered model
Total pore volume (Å ³)	5540.72	6199.09
Total pore volume (cm ³ ·g ⁻¹) Connolly surface	0.901	1.01
Total pore volume percentage (%)	63	70
Surface area (m ² ·g ⁻¹)	3585.74	3238.19
Sphere Diameter (Eq. to V_{oct})	17 Å	
Sphere Diameter (Eq. to V_{tet})	10.2 Å	

5.3 Thermogravimetric analysis

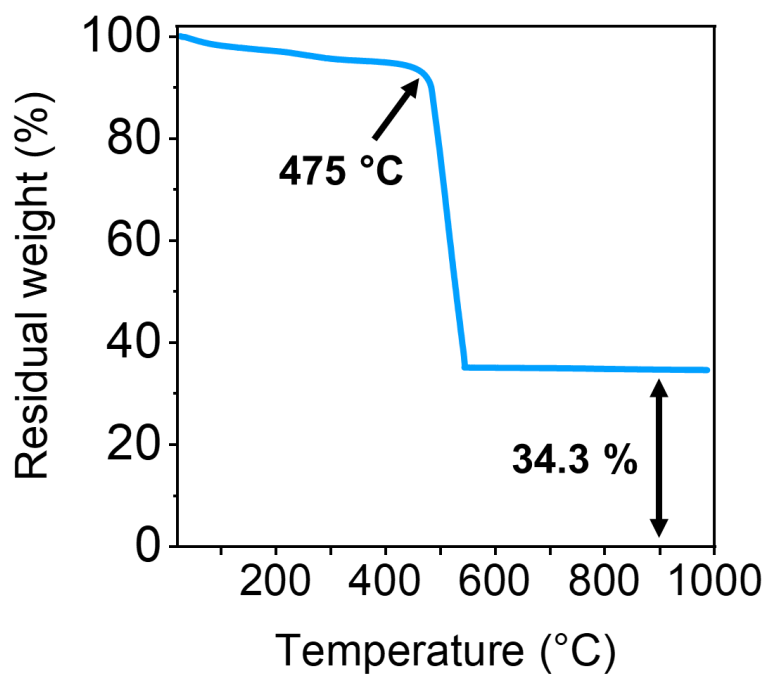


Figure S21 | Thermogravimetric analysis of Hf-DPA. The measurement was performed between 30 °C and 1000 °C under oxidative conditions (dry air stream, 50 mL/min). The framework display thermal stability up to 475 °C. The experimental residue (34.3 % residual mass) agrees with the theoretical value (34.1 %) expected for formation of pure HfO₂ after thermal treatment.

5.4 Infrared spectroscopy

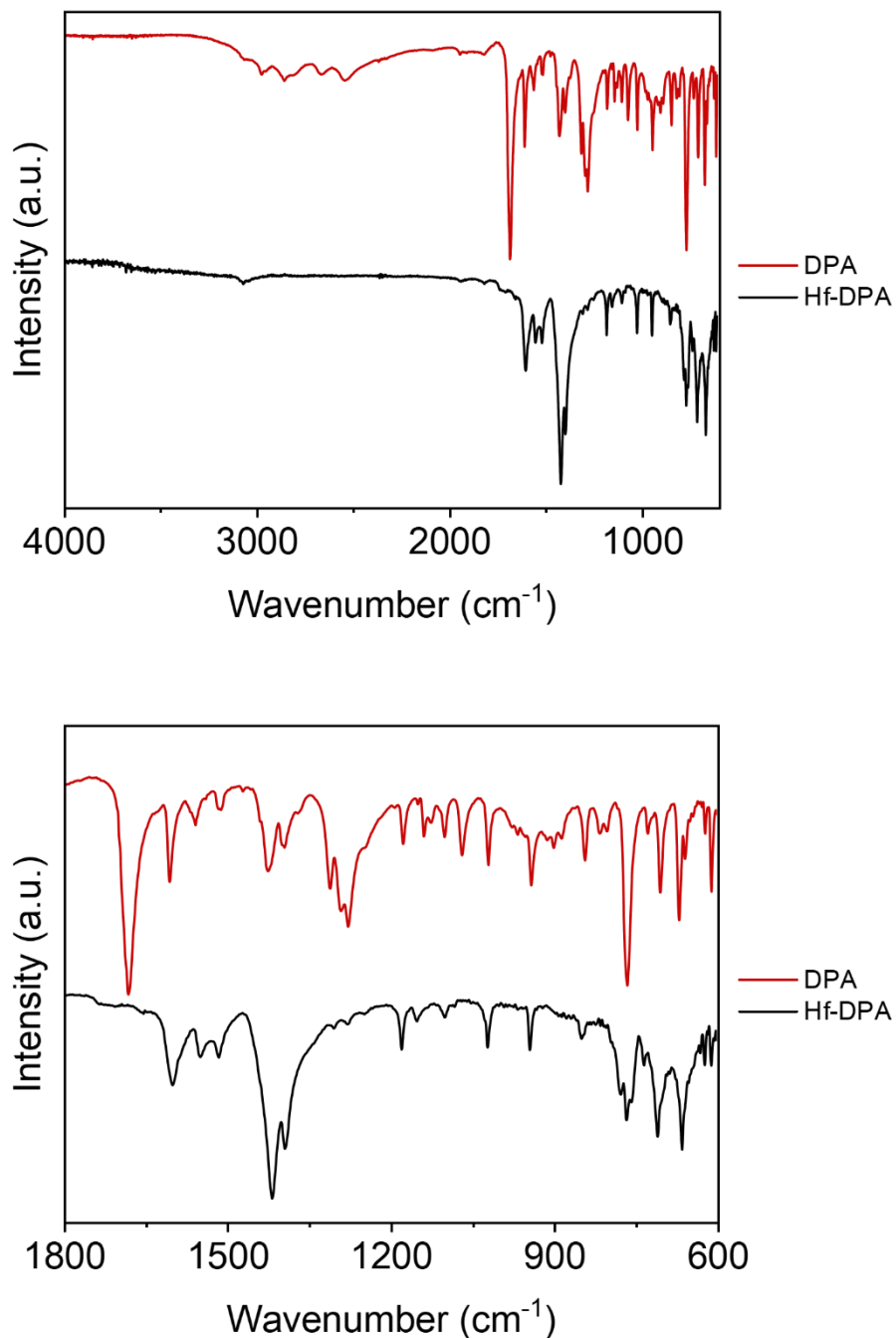


Figure S22 | Top: FT-IR spectra of 9,10-bis(4-carboxyphenyl)anthracene (DPA) ligand and Hf-DPA between 4000 cm⁻¹ and 600 cm⁻¹. Bottom: FT-IR spectra of 9,10-bis(4-carboxyphenyl)anthracene (DPA) ligand and Hf-DPA between 1800 cm⁻¹ and 600 cm⁻¹. The C=O stretching band of the free carboxylic acid (1684 cm⁻¹) shifts to 1602 cm⁻¹ after coordination with Hf⁴⁺ ions.

5.5 Liquid state ^1H -NMR of digested Hf-DPA

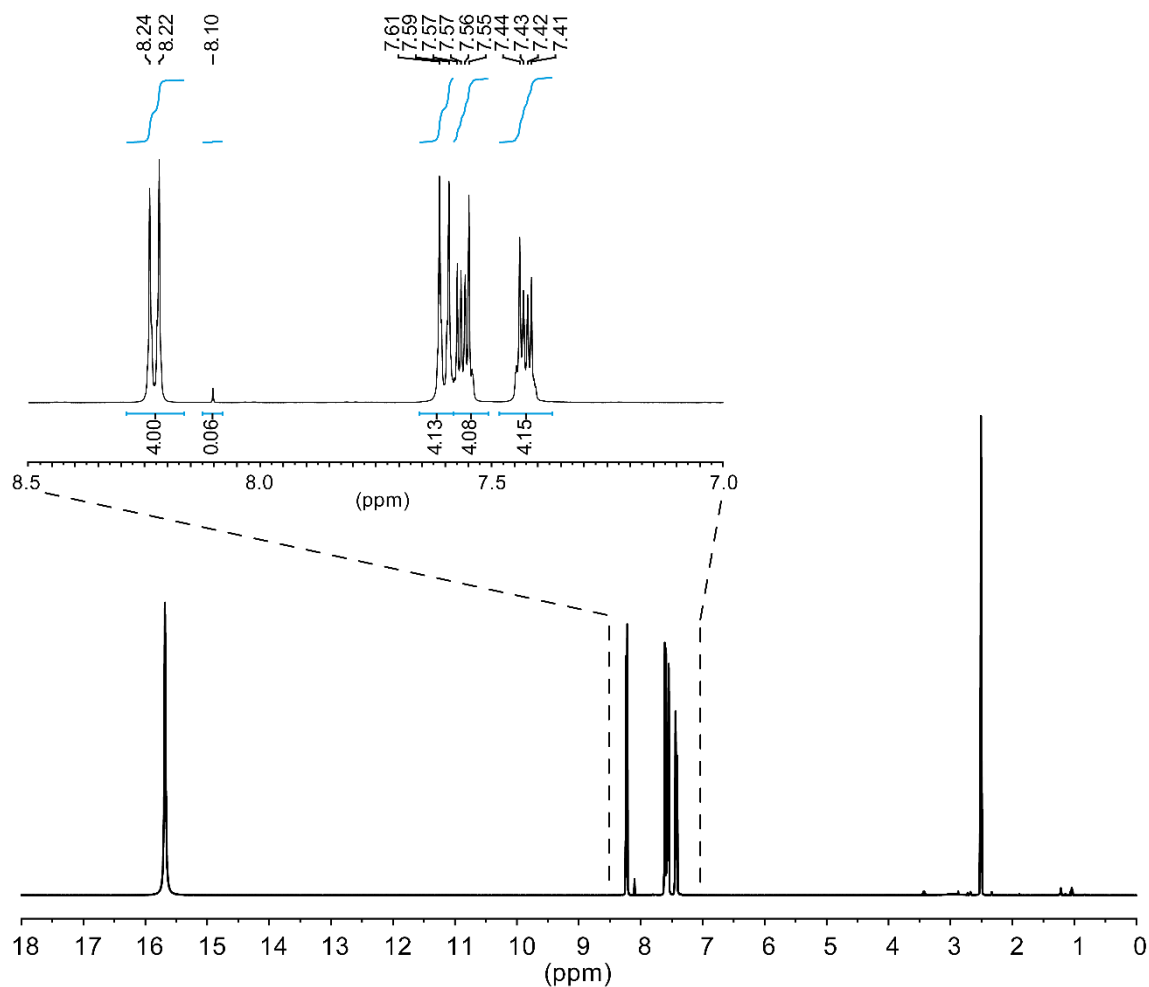


Figure S23 | ^1H liquid NMR of digested Hf-DPA MOF. Sample preparation: the activated Hf-DPA sample (5.0 mg) was dispersed in DMSO-d_6 (0.2 mL) and 0.1 mL of deuterated trifluoroacetic acid was added. The mixture was sonicated for 1 minute and then 0.8 mL of DMSO-d_6 was added and ^1H liquid NMR was collected. The spectrum was collected on a AVANCE NEO Bruker instrument (400 MHz) at 298.1 K in DMSO-d_6 . The peaks match the signal from DPA ligand. A signal at 8.10 ppm is assigned to formic acid (the monocarboxylic acid used as modulator during MOF synthesis) that is included as an impurity coordinated to the Zr-based clusters ($\sim 6\%$ as quantified from integration of the ^1H liquid NMR spectrum).

5.6 Solid state NMR

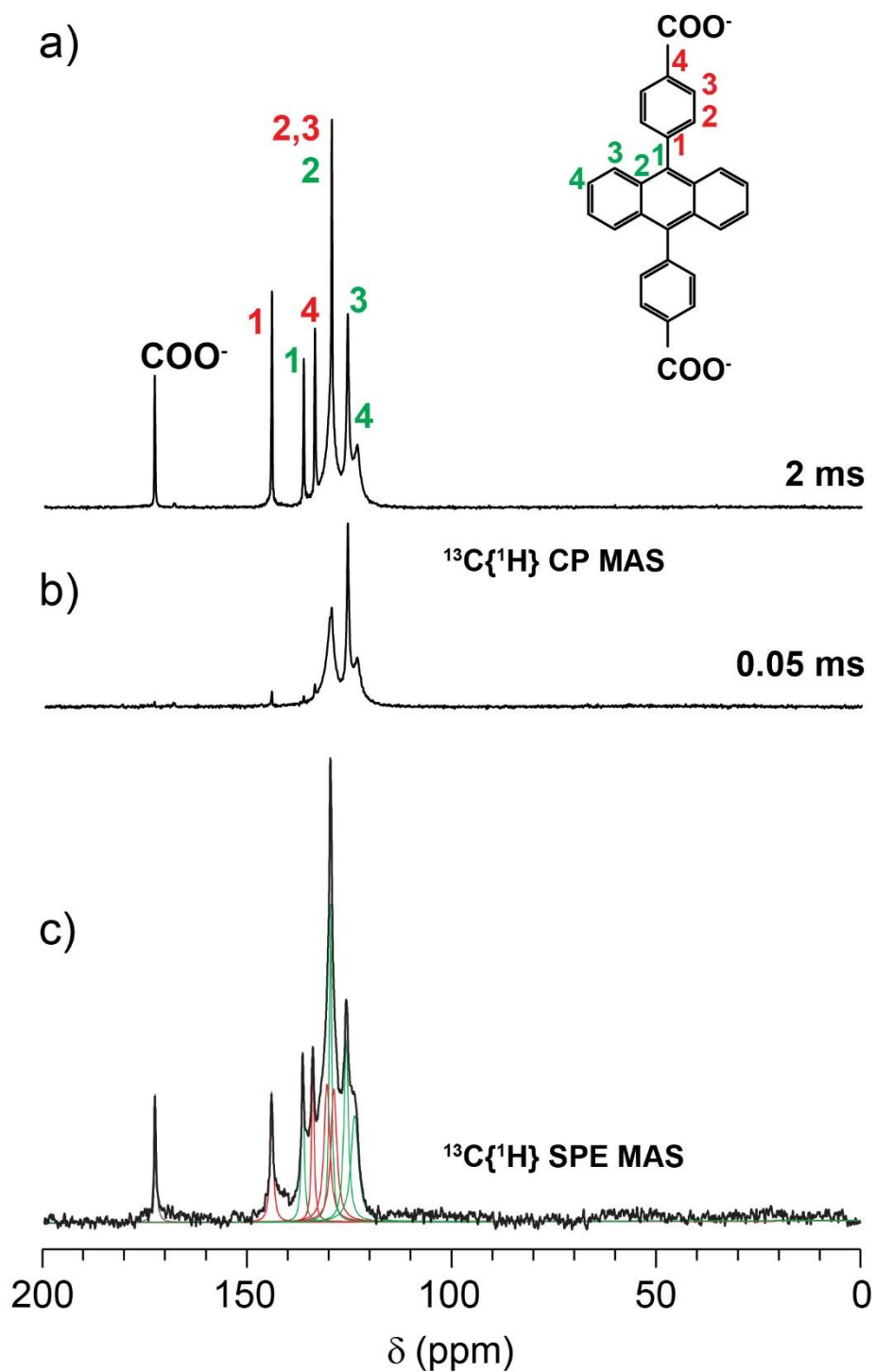


Figure S24 | ^{13}C MAS NMR analysis of Hf-DPA MOF performed at 298 K at a spinning speed of 12.5 kHz: $^{13}\text{C}\{^1\text{H}\}$ CP spectra collected with contact time of 2 ms (a) and 0.05 ms (b). (c) Quantitative $^{13}\text{C}\{^1\text{H}\}$ SPE MAS spectrum collected with a recycle delay of 60 s; the spectral profile was simulated by Lorentzian line shapes.

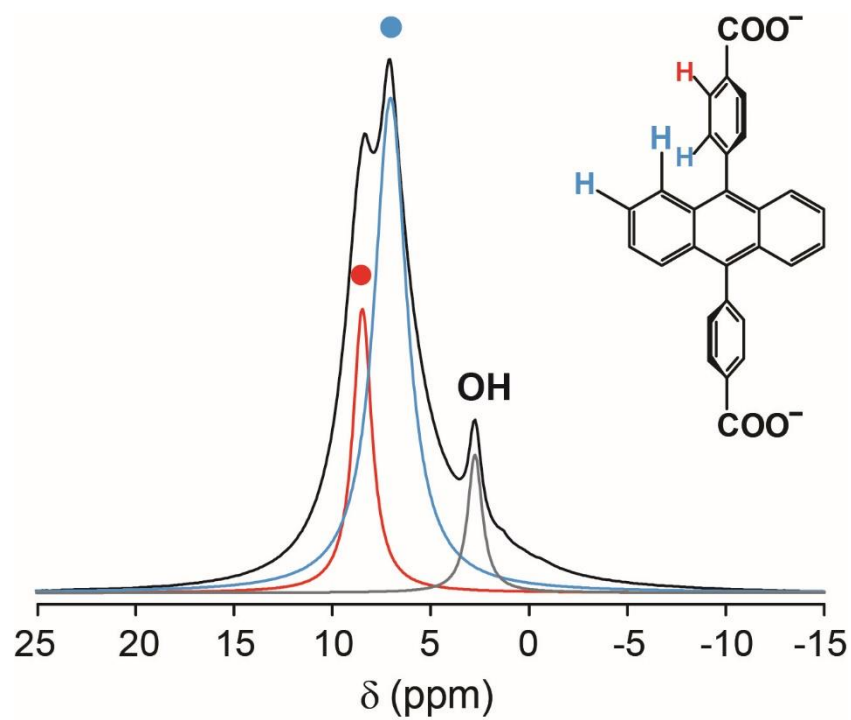
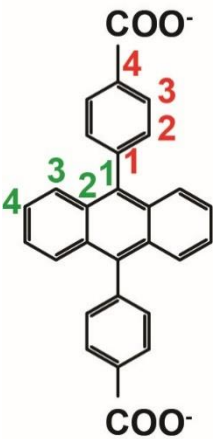
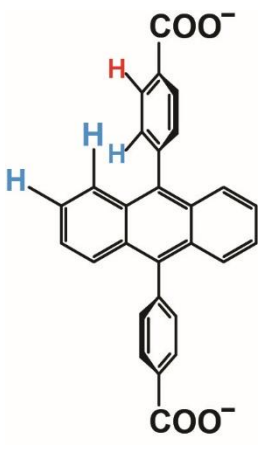


Figure S25 | Quantitative ¹H SPE MAS spectrum of Hf-DPA collected at 298 K at 7.04 T with a spinning speed of 12.5 kHz and a recycle delay of 20 s; the spectral profile was simulated by Lorentzian line shapes.

Table 4. ^{13}C and ^1H chemical shifts of Hf-DPA MOF from solid state NMR spectra collected at 7.04 T and 298 K.

Hf-DPA	Assignment	δ (ppm)	Amount %
	C_1	136.6	7.3
	C_2	129.8	14.6
	C_3	126.0	14.5
	C_4	123.9	14.5
	C_1	144.2	7.3
	$\text{C}_2 - \text{C}_3$	130.7 - 129.0	14.6 - 14.6
	C_4	134.2	7.3
	COO^-	172.8	5.3 (underestimated)
	H	8.45	22.8
	H	7.02	68.5
	$-\text{OH}$	2.73	8.7

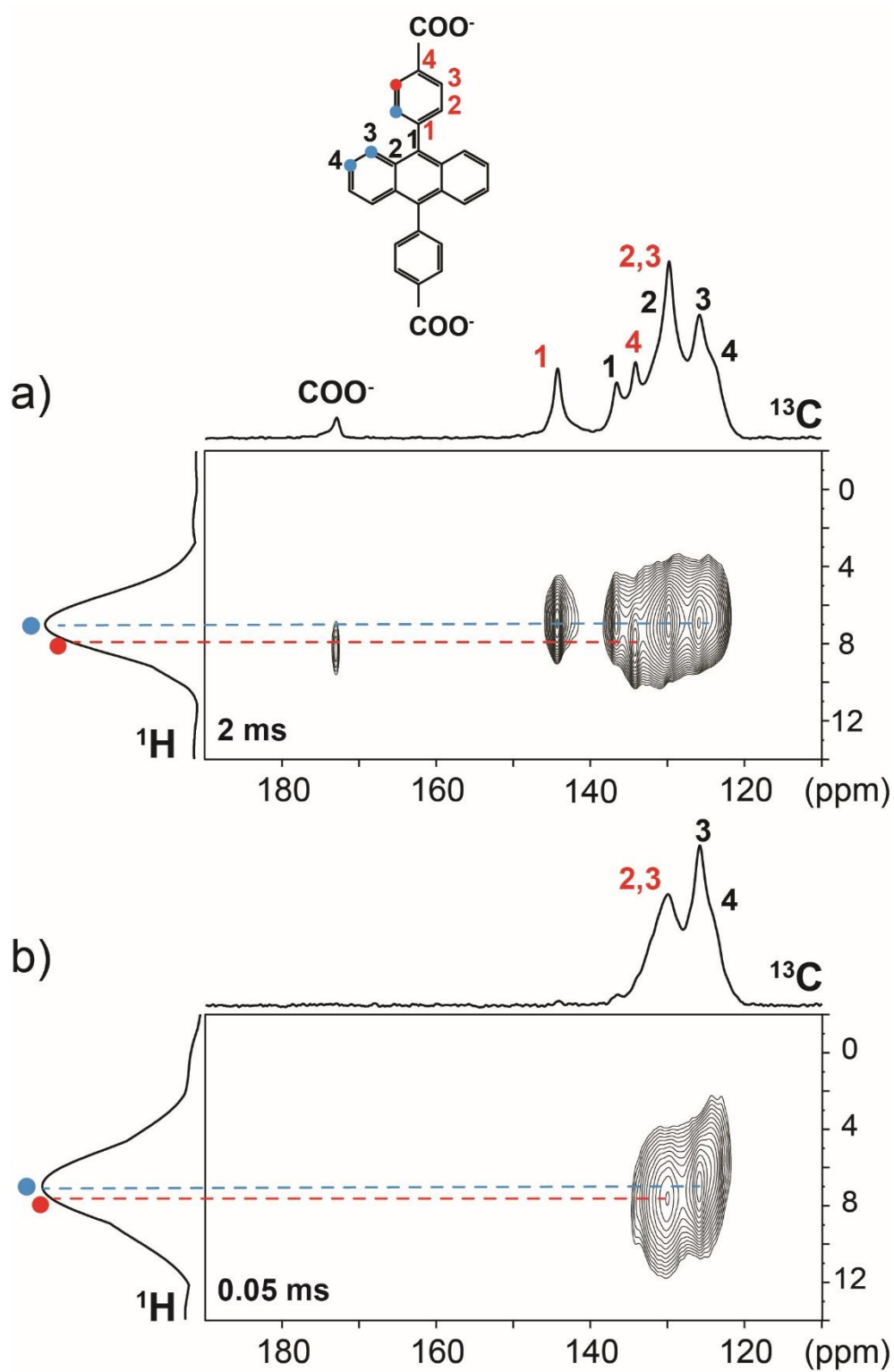


Figure S26 | 2D ^1H - ^{13}C PMLG HETCOR NMR spectra of Hf-DPA MOF collected at 298 K, at a spinning speed of 12.5 kHz and contact times of 2 ms (a) and 0.05 ms (b).

Table 5. Hyperpolarized ^{129}Xe chemical shifts and peak intensity of Hf-DPA from spectra collected at different temperatures.

Temperature	^{129}Xe in pores		Free ^{129}Xe gas	
	δ (ppm)	Amount (%)	δ (ppm)	Amount (%)
293	97.7	84	0	16
248	100.5	91	0	9
202	102.5	95	0	5
195	104.6	95	0	5
187	108.8	95	0	5

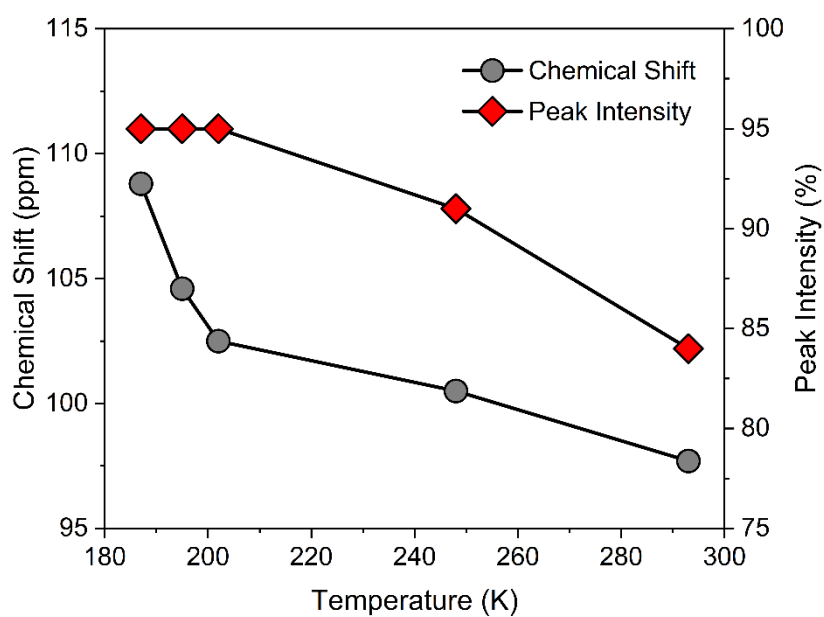


Figure S27 | ^{129}Xe peak intensity and chemical shifts versus temperature.

5.7 Gas adsorption analysis

N₂, Ar and Kr adsorption isotherms collected at 77 K proved the open porosity and pore accessibility of Hf-DPA to gases.

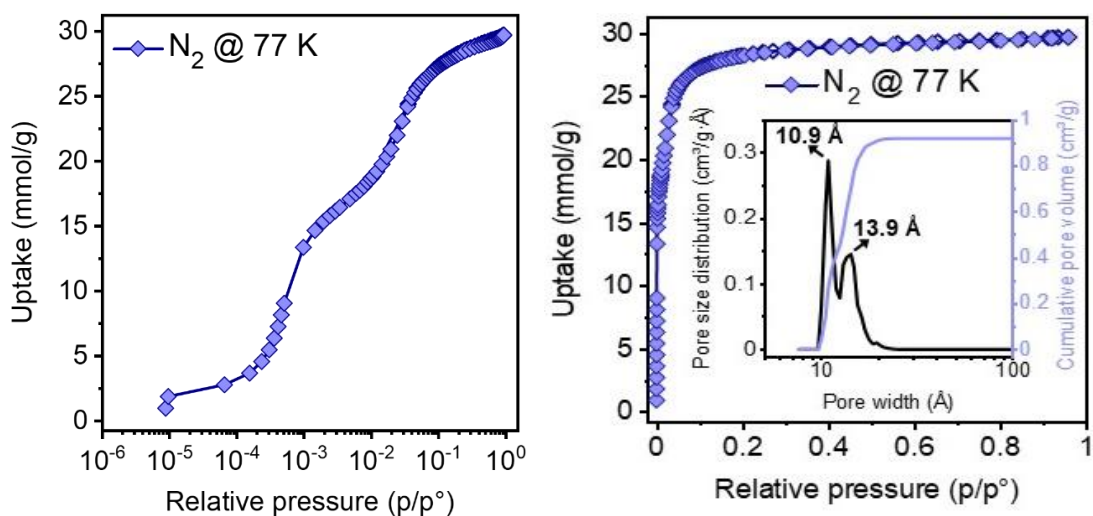


Figure S28 | N₂ adsorption isotherm of Hf-DPA collected at 77 K in logarithmic scale.

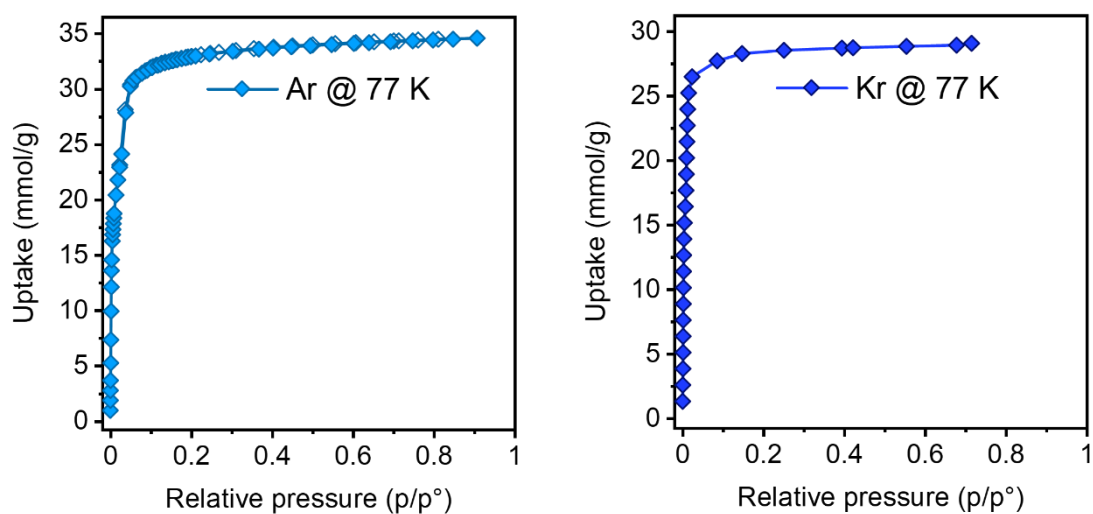


Figure S29 | Ar and Kr adsorption isotherms of Hf-DPA collected at 77 K.

Ar and Kr isotherms were also collected at 298 K and low pressure. They display linear uptake with pressure (Henry isotherm).

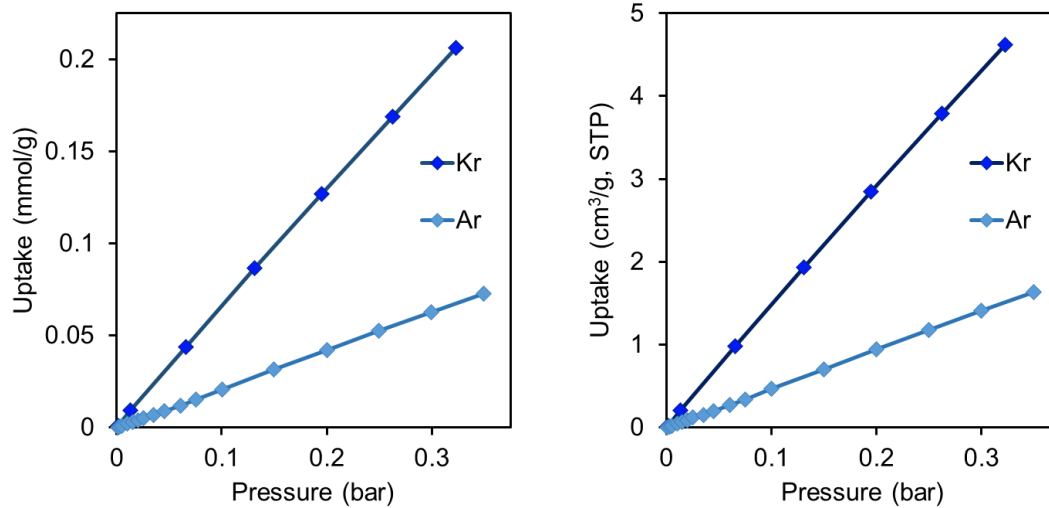


Figure S30 | Ar and Kr adsorption isotherms of Hf-DPA collected at 298 K up to 0.3 bar.

6. TIME RESOLVED PHOTOLUMINESCENCE DATA ANALYSIS

The time resolved photoluminescence (PL) spectra and scintillation data discussed in the main text show in general a complex behavior. The signal decay has been reproduced with an analytical multi-exponential function

$$I_{PL}(t) \propto \sum_i A_i e^{-(t/\tau_i)}. \quad \text{Eq. S1}$$

The parameters used for the fitting procedure are reported in Table 2. The characteristic emission lifetime τ_{avg} has been calculated as the weighted average of the characteristic decay time for each i -exponential function by

$$\tau_{avg} = \frac{\sum_i A_i \tau_i}{\sum_i A_i}. \quad \text{Eq. S2}$$

Table 6. Fit parameters employed to analyze the time resolved photoluminescence intensity decay spectra recorded on Hf-MOFs dispersions in THF and bare powders.

@ max PL	τ (ns)	A ₁	τ (ns)	A ₂	τ (ns)	A ₃	τ_{avg} (ns)
Hf-MOF							
THF 300 K	2.5	0.97	8.8	0.03	-	-	2.8
THF 77 K	1.3	0.19	3.2	0.53	4.9	0.28	3.3
powder 300 K	0.6	0.23	2.3	0.66	6.6	0.11	2.4
powder 77 K	1.7	0.43	5.0	0.57	-	-	3.6
@ max Scint.							
powder	1.4	0.69	4.6	0.26	18.7	0.05	3.0

7. PHOTOLUMINESCENCE QUANTUM YIELD MEASUREMENTS

The fluorescence quantum yield ϕ_{pl} of MOF nanocrystals dispersions has been determined by relative method for yield measurements. The ϕ_{pl} was determined relative to 10^{-5} solution of DPA in cyclohexane ($\phi_{std}=0.96$),¹² which has used as secondary standard according to the following equation

$$\phi_{unk} = \phi_{std} \left(\frac{A_{std}}{A_{unk}} \right) \left(\frac{I_{unk}}{I_{std}} \right) \left(\frac{P_{std}}{P_{unk}} \right) \left(\frac{\eta_{unk}}{\eta_{std}} \right)^2, \quad \text{Eq. S3}$$

where ϕ_{unk} , A_{unk} , I_{unk} , P_{unk} and η_{unk} represent the quantum yield, absorbance at the excitation wavelength of 370 nm, integrated photoluminescence spectral profile, excitation power density, and refractive index of the investigated material. The corresponding terms for the subscript “std” are for the reference quantum counter DPA at the identical excitation wavelength. To avoid any detrimental effect of the scattering of the excitation light that could avoid a proper determination of the samples absorbance, the absorption spectrum of MOF dispersion has been measured using an integrating sphere. The ϕ_{pl} of dicarboxyl-DPT in diluted solution has been measured using the Rhodamine 6G in ethanol (10^{-5} M, $\phi_{std}=0.95$) as secondary standard.¹³

8. TEMPERATURE DEPENDENT SPECTROSCOPY

Table 7. Luminescence spectral parameters as a function of the temperature for Hf-MOF nanopowders.

Temperature	max PL (nm)	max RL (nm)	FWHM (eV) PL	FWHM (eV) RL
300 K	496	498	0.56	0.53
10 K	485	490	0.50	0.48

Glow curve analysis. We make a qualitative evaluation of the influence of defects in the scintillation performance of MOF nanocrystals by their RL and TSL response. We acquired the radioluminescence signal at 10 K emitted during the irradiation preceding the TSL measurement as a function of cumulated dose (proportional to the exposure time since a constant dose rate of 8 mGy/s was used): the integral of the radioluminescence emission over dose (I_{RL}) is due to the prompt recombination of free carriers generated by irradiation up to a total X-ray dose of around 10 Gy. Conversely, the integral of the glow curve (I_{TSL}), acquired after the aforementioned irradiation at 10 K, is related to the delayed recombination of previously trapped charge carriers thermally released upon heating. We could estimate the amount of light originating from the thermal release of trapped carriers and not contributing to the prompt scintillation response by calculating

$$T_{\%} = \frac{I_{TSL}}{I_{RL} + I_{TSL}}$$

where I_{TSL} and I_{RL} have been previously defined. Our approach allows to evaluate in an operative way the contribution of trapping phenomena with respect to prompt scintillation. We directly compare the $T_{\%}$ of our systems with that of standard reference organic scintillators. We obtain $T_{\%} = 2.5 \%$ for Hf-based MOF nanocrystals and $T_{\%} = 0.4 \%$ for EJ-276.

9. COMPARATIVE RADIOLUMINESCENCE EXPERIMENTS

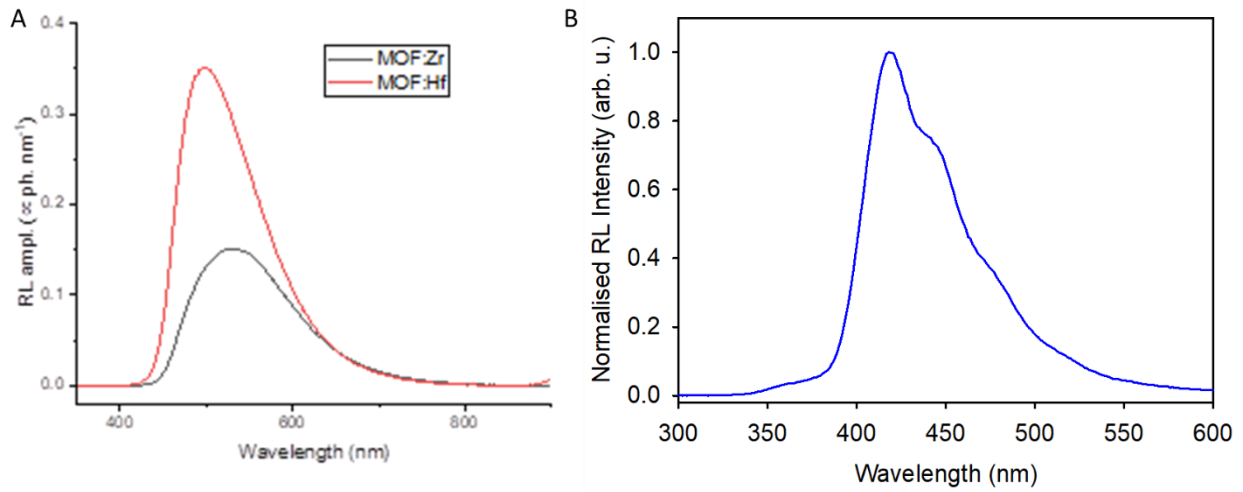


Figure S31 | Radioluminescence spectra of Hf-MOFs and Zr-MOFs powders (A) and polystyrene microspheres (B) under soft X-ray irradiation.

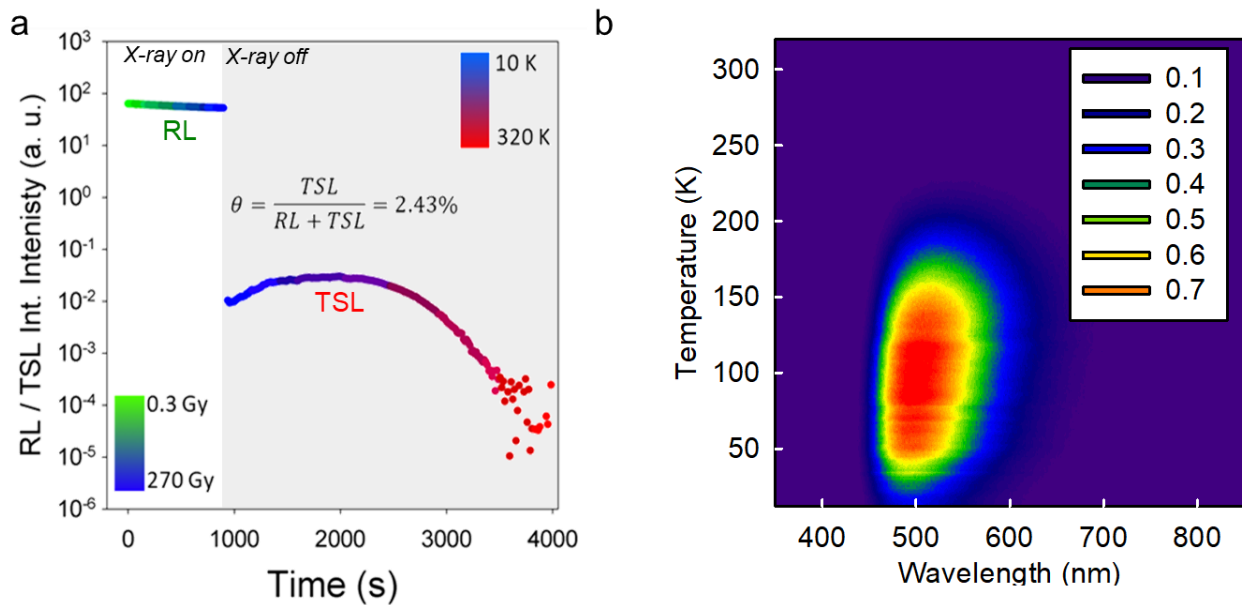


Figure S32 | (a) RL intensity as a function of cumulated dose (green dots) delivered in 900 s and TSL intensity (red dots). (b) Contour plot of wavelength-resolved TSL intensity.

10. GRAND CANONICAL MONTE CARLO (GCMC) GAS ADSORPTION SIMULATIONS

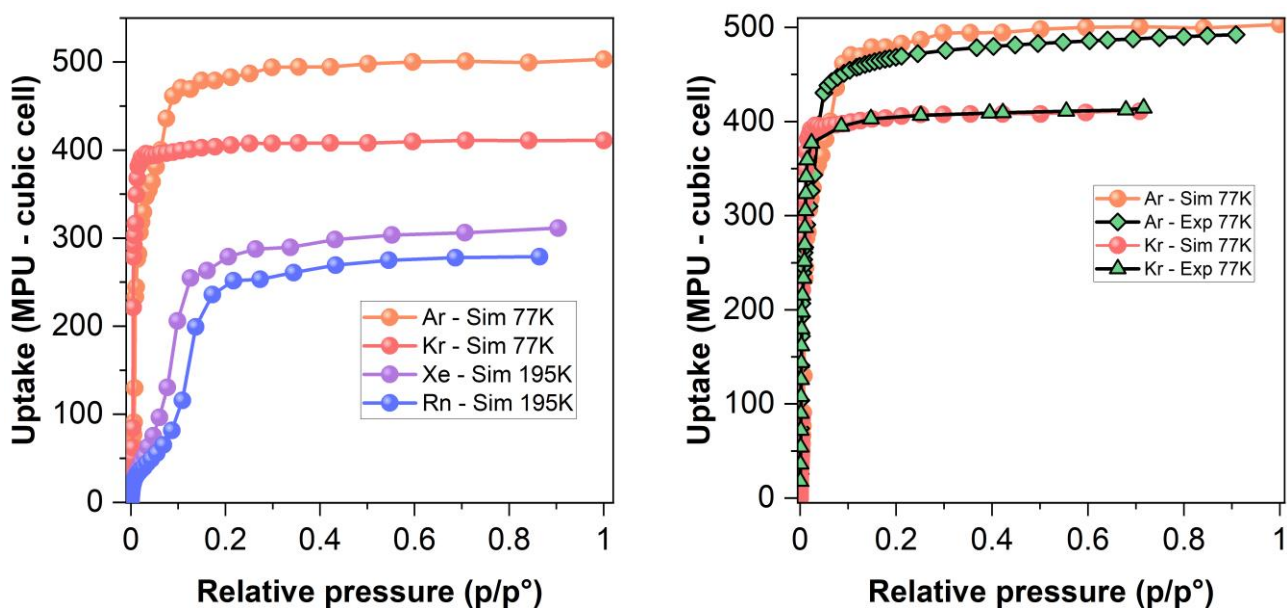


Figure S33 | GCMC simulated adsorption isotherms of Ar, Kr, Xe and Rn for a cubic unit-cell of Hf-DPA ($32.79 \text{ \AA} \times 32.79 \text{ \AA} \times 32.79 \text{ \AA}$). The simulation for Ar and Kr were performed at 77 K while those for Xe and Rn were performed at 195 K. Ar and Kr are shown together with their respective experimental adsorption isotherms at 77 K for comparison. The uptake is expressed in molecules per unit-cell (MPU)

Table S8. The maximum gas uptake for the noble gasses at low temperatures, 77 k for Ar and Kr, and 195 K for Xe and Rn (GCMC simulated). Only Ar and Kr experimental data have been acquired and shows good comparison to the simulated values.

	Ar	Kr	Xe	Rn
Max Loading EXP (mmol/g)	35	29	N.A.	N.A.
Max Loading EXP (MPU - Hf-DPA cubic cell)	492	414	N.A.	N.A.
Max Loading Sim (MPU - Hf-DPA cubic cell)	499	410	311	279
Density of gas absorbed (g/mL)	1.333 ^a	2.301 ^a	2.735 ^a	4.148 ^a
Liquid density (g/mL)	1.417 ^a	2.41 ^a	2.95 ^a	4.4 ^a

a – The densities of the absorbed gasses were calculated from the total molar mass of absorbed gas ($\text{MPU}_{\text{max}} \cdot M_w$ - g/mol) divided by the pore volume in mL/mol ($\text{NA} \cdot V_{\text{pore}} \cdot 10^{-24}$).

b – These are the liquid densities of the noble gasses at their respective boiling points; 83.8 K, 119.8 K, 165.1 K, 221.35 K for Ar, Kr, Xe and Rn respectively. {Haynes, 2016 #197}

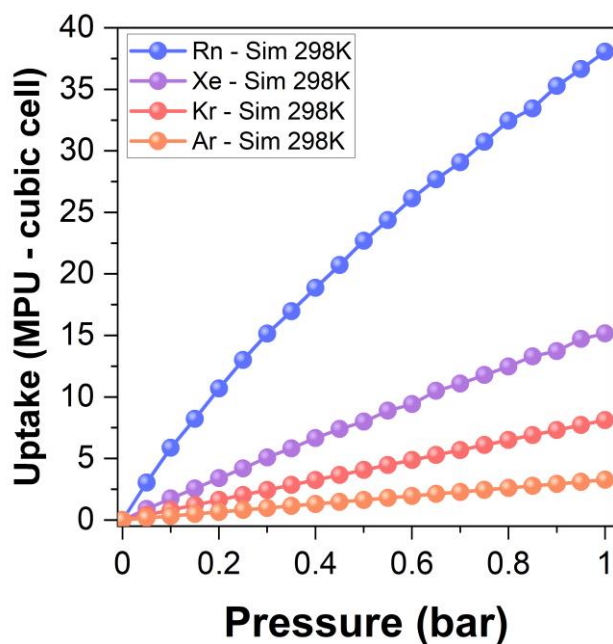
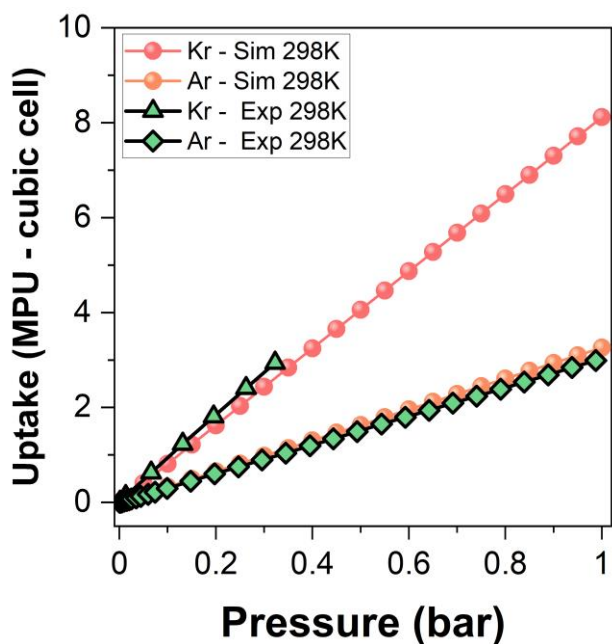


Figure S34 | Room temperature GCMC simulated adsorption isotherms of Ar, Kr, Xe and Rn for a cubic unit-cell of Hf-DPA (32.79 Å × 32.79 Å × 32.79 Å). Ar and Kr are shown together with their respective experimental adsorption isotherms collected at 298 K for comparison. The uptake is expressed in molecules per unit-cell (MPU)

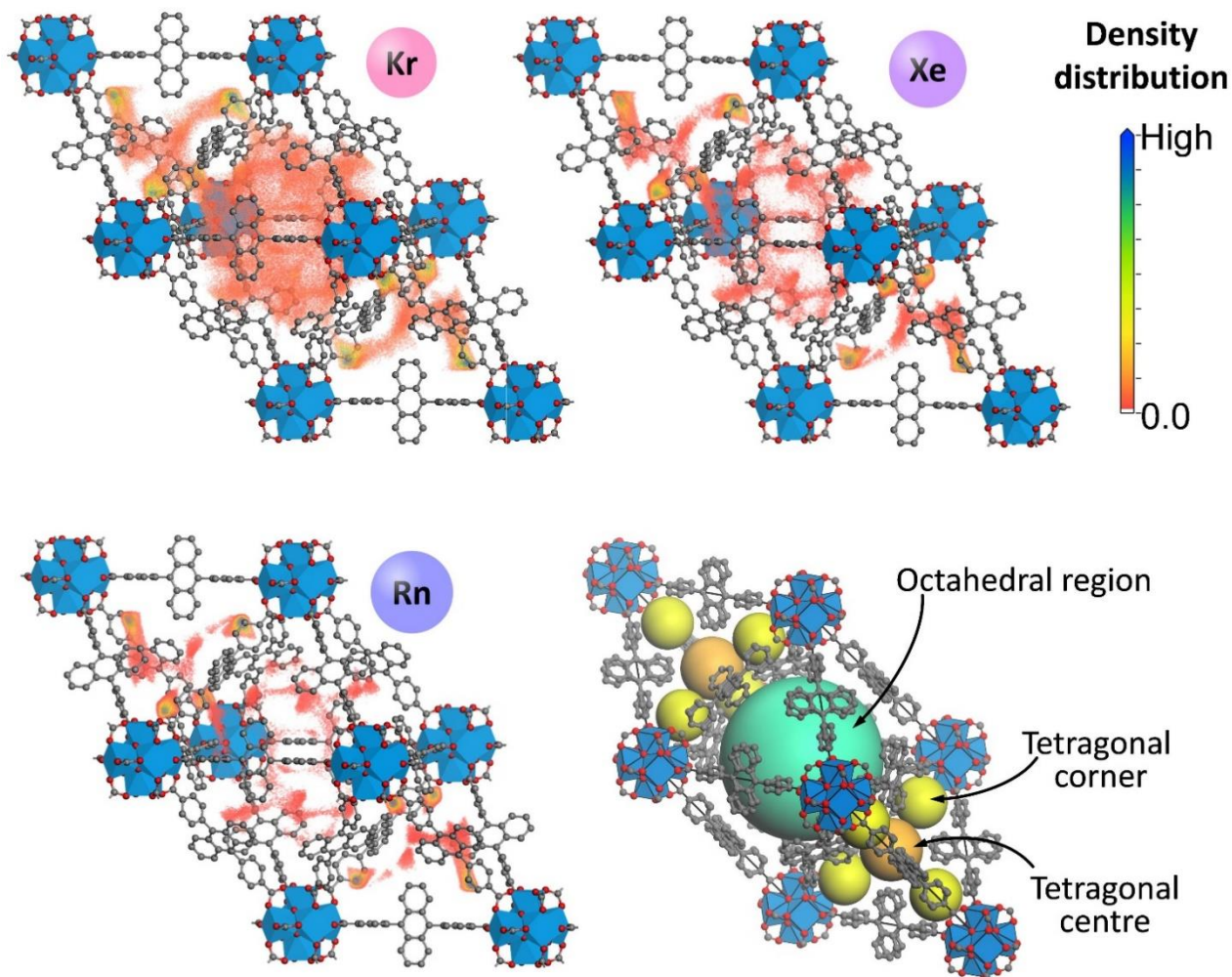


Figure S35 | Gas density distributions calculated at 5 kpa (0.05 bar) and 298 K using fixed pressure GCMC adsorption simulations for Kr, Xe and Rn using the primitive unit-cell of Hf-DPA. Red indicated very low density while blue indicates the highest. The use of the primitive cell allows for better visualization of the pore occupancy. The spherical representation of the different pores are shown to more easily correlate the pores with the density distribution.

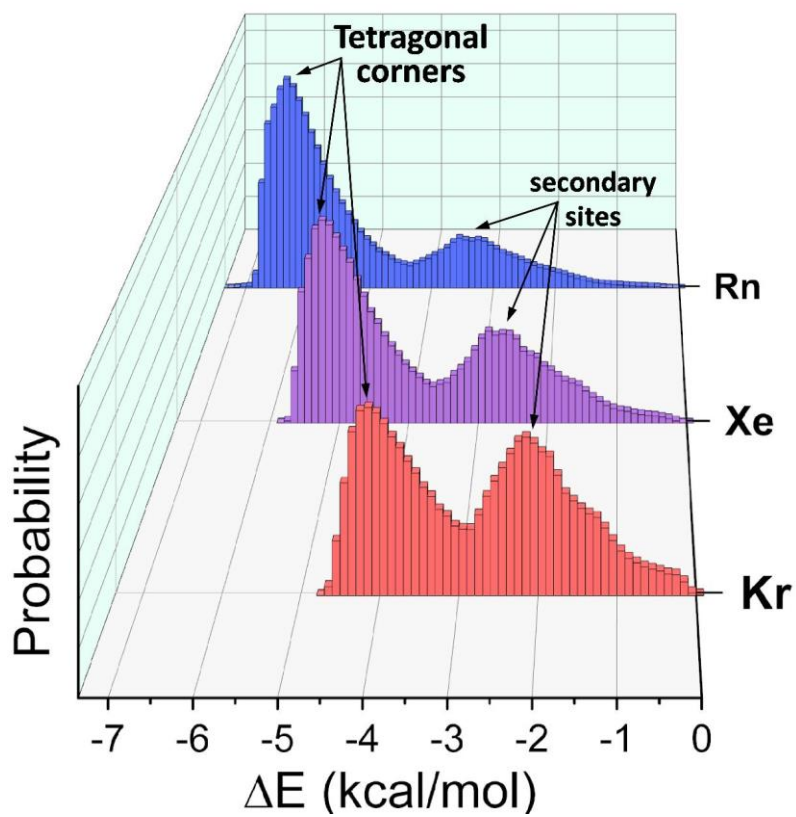


Figure S36 | Energy distributions obtained from the fixed pressure GCMC adsorption simulations, performed at 5 kpa (0.05 bar) and 298 K, for Kr, Xe and Rn.

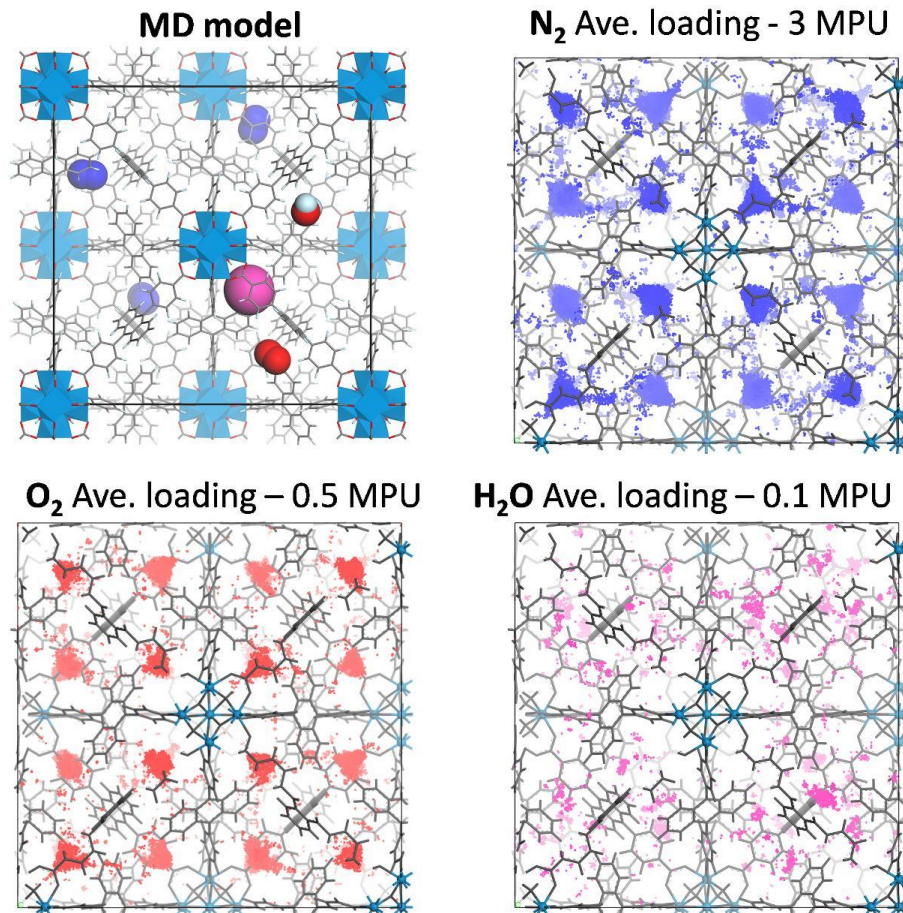


Figure S37 | GCMC fix pressure sorption simulation at 1 bar, 298 K considering N₂ (76%), O₂ (21%), H₂O (3%) as the air composition. Top-Left shows a snapshot from the GCMC simulation with an Krypton atom (magenta) added for a dynamics simulation at 298 K, from which the mean-square-displacement (MSD) could be determined.

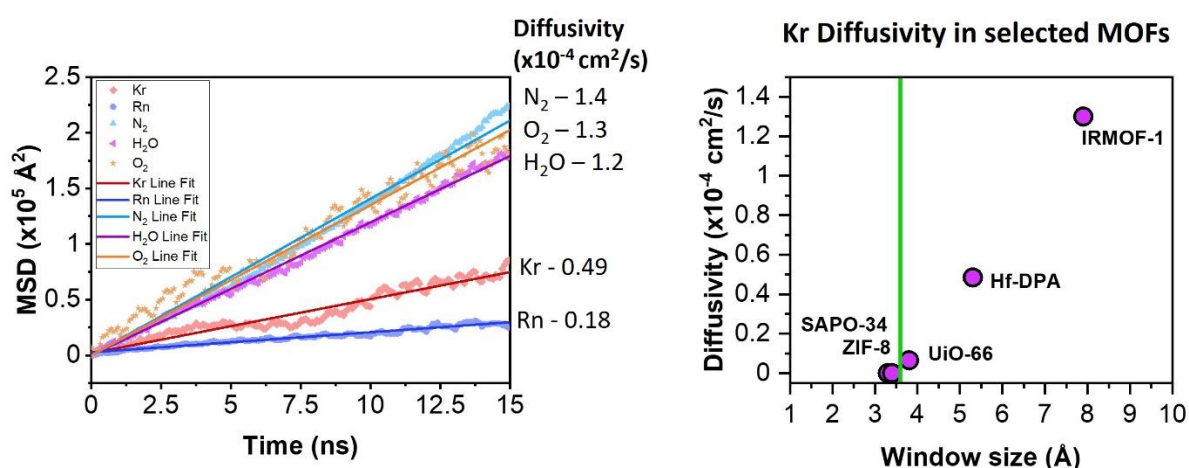


Figure S38 | Left – The MSD vs. time extracted from a 15 ns MD simulation used to determine the diffusivity of the Kr in an air loaded Hf-MOF. Right – A plot of Krypton diffusivity against average window size of the porous materials for comparison against Hf-DPA. {Anderson, 2018 #198} The Kr diffusivity has a linear correlation to the average window size of the MOFs.

11. TRIPLE TO DOUBLE COINCIDENCE TECHNIQUE

The triplet to double coincidence technique (TDCR) method is widely used by national metrology institutes for primary standardization of liquid scintillators counters ¹⁴ It is especially suited for the determination of the activity of pure beta emitters. The method is based on a model that provides a statistical description of the physical phenomena occurring in the LSC system. With the TDCR method, one can obtain the detection efficiency of the detector from the ratio of the triple to double coincidences. The application of the method requires the use of a specialized counter with three PMTs, in our case the portable micro-TDCR up to now the most efficient developed,¹⁵ and electronics that is able to record the triple (T) and double (AB , BC , AC) coincidences counting rates, in our case a LabZY nanoTDCR. ¹⁶ A logical sum of double coincidences (D) channel is also used in order to measure the counting rate of the system and calculate activity. Under the assumption of three identical PMTs and a Poisson distribution law for the detection probability, the ratio of the detection efficiency in the T and D channel is defined by the equation:

$$\frac{\varepsilon_T}{\varepsilon_D} = \frac{\int_{\text{spectrum}} S(E) \left(1 - e^{-\frac{\nu \alpha m(E)}{3}}\right)^3}{\int_{\text{spectrum}} S(E) \left(3 \left(1 - e^{-\frac{\nu \alpha m(E)}{3}}\right)^2 - 2 \left(1 - e^{-\frac{\nu \alpha m(E)}{3}}\right)\right)^3}$$

where α is the scintillation yield (photon \cdot keV⁻¹), ν is the PMT quantum efficiency, $m(E)$ is the non-linearity model of the scintillator (for example Birks) ¹⁷ and $S(E)$ is the emission spectrum of the radionuclide. The number 3 in the denominator of the equations is due to the 1/3 symmetry of the device.

For a large number of detected events the ratio of the T to D coincidences tends towards the ratio of the detection efficiencies or $T/D = \varepsilon_T / \varepsilon_D$. Note that in the case of non-identical PMTs a set of three equations must be used, including the relative efficiencies of the three PMTs (T/AB , T/BS , T/AC). {Kossert, 2020 #196} In the framework of this study we use this ratio as an indicator of efficiency. This is possible as we use between each experiment the same device, the same scintillator configuration (same volume, both in powder form) and the same gas. We can thus compare the results between the two materials knowing that the remaining common parameter will be the yield and scintillator non linearity ($\alpha m(E)$). If this ratio is close to one that means we reach the maximum efficiency for this configuration, thus we have a very good material. On the other hand, if it is not close to one, that means either we have a loss of light due to diffusion in the material, a scintillation yield that is too weak or an energy transfer between radiation and the scintillator that is not optimized.

TDCR analysis. The counter efficiency indicator η is calculated as the ratio between the triple coincidence (T) and double coincidence (D) counting rates. Thus the T/D ratio data (Figure S42) gives us an indication of the detection efficiency; with this indicator for a same isotope, we are directly comparing the product of the scintillation yield and PMTs quantum efficiency. Here we obtain a very similar value around 0.2-0.3 for both two coincidence windows analyzed and for both the two materials PS microspheres and Hf-DPA porous nanocrystals. Specifically, The Hf-DPA presents an efficiency indicator 4.2% lower than microspheres that does not correspond to the difference of 30% due to the PMTs quantum efficiency and wavelength emission of both scintillators. This means that Hf-DPA is providing a high scintillation yield than PSm. This combined analysis of the efficiency indicator η and the D count rate value indicate that Hf-DPA detects a greater quantity of events than PS microspheres. We ascribe this improved detection to an improved interaction with the electron emitted by the radionuclides thanks to the more adsorption of the gas in the pores that enhances the interaction of β particle with the heavy elements of framework increasing the scintillation output.

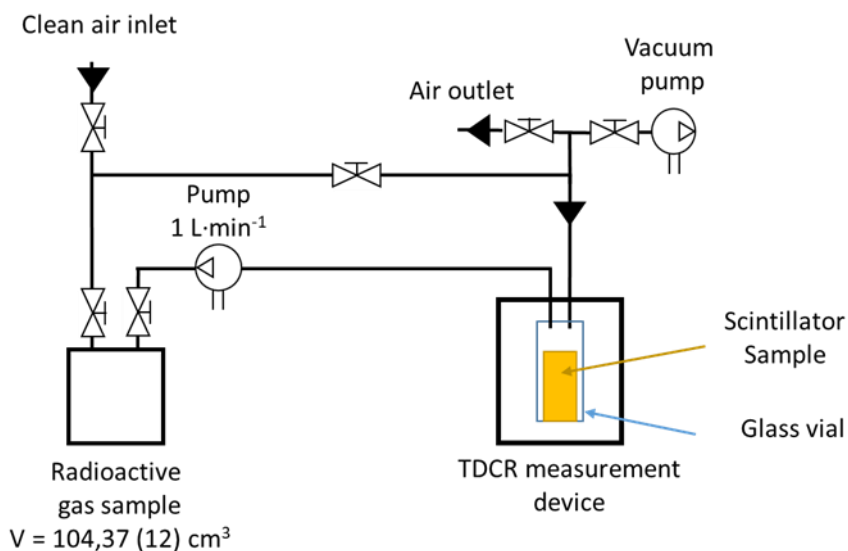


Figure S39 | Electrical scheme of the time coincidence-based detector for radionuclides gases exploiting porous nanoscintillators.

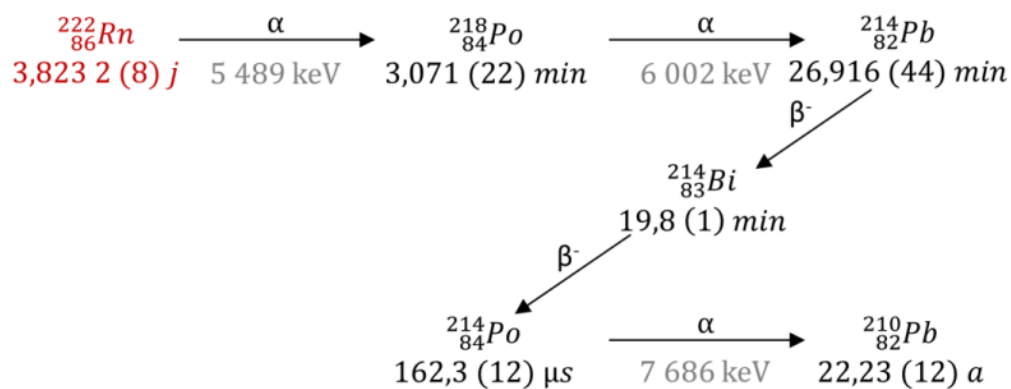


Figure S40 | Radioactive decay chain of ²²²Rn.

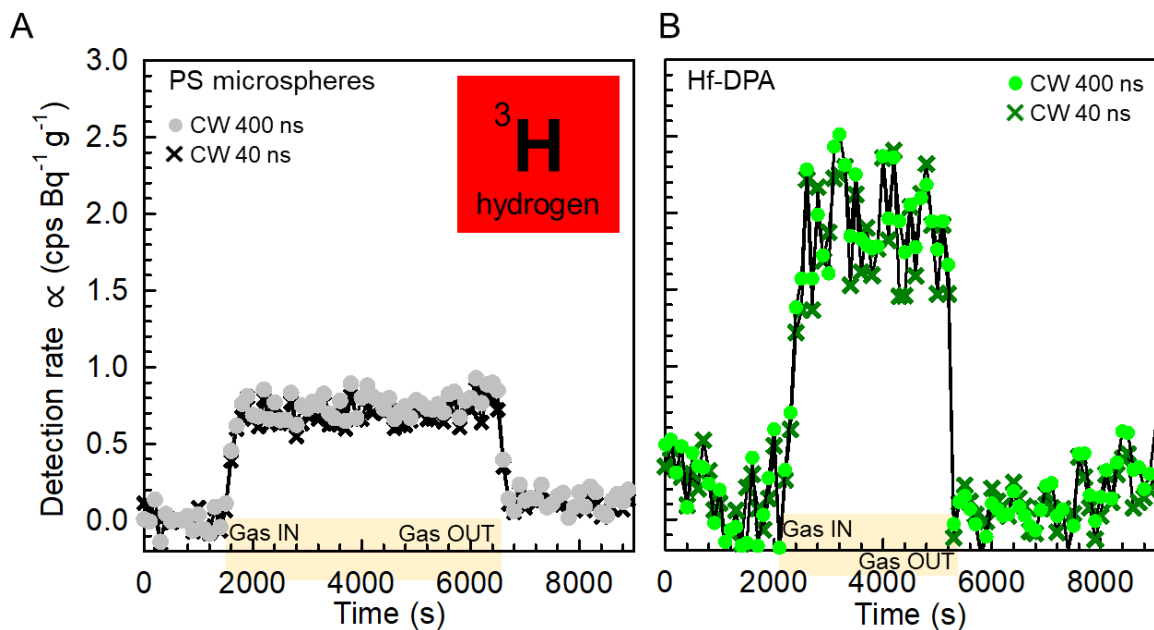


Figure S41 | (A) Double coincidence detection of ^3H by polystyrene (PS) microspheres powder (left) and Hf-DPA nanocrystals powder (right) using two different coincidence windows (CW) for detection (40 ns and 400 ns). The shaded stripes indicate when the radioactive gas has been injected in the detection device (Gas IN) and then washed out by a flux of clean air (Gas OUT).

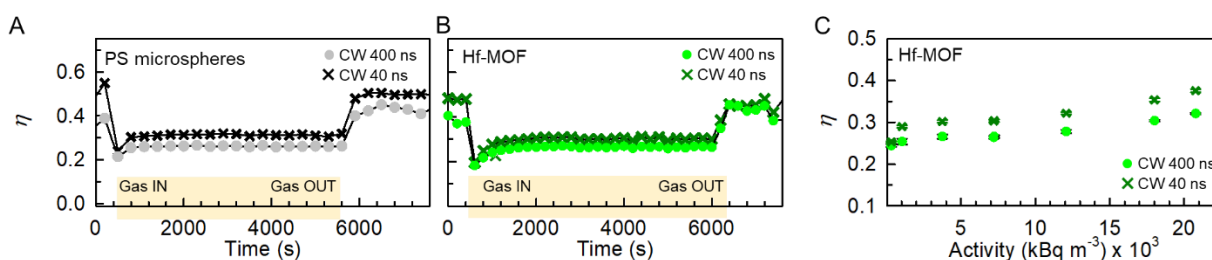


Figure S42 – Radioactive ^{85}Kr gas detection by porous Hf-DPAs scintillating nanocrystals. Detection efficiency of ^{85}Kr by PS microspheres powder (A) and Hf-DPA nanocrystals powder (B) using a CW of 40 ns and 400 ns. (C) Detection efficiency of ^{85}Kr by Hf-DPA nanocrystals powder as function of the sample activity.

12. GAS DETECTION DATA REPRODUCIBILITY

GAS DETECTION DATA REPRODUCIBILITY

To verify the reproducibility of the measurements and of the obtained results, several cycles of exposure to a ^{85}Kr atmosphere and rinsing with clean air were performed. The results presented in Table 3 are compatible within their standard uncertainties (which means at confidence intervals $k = 1$, and correspond to a relative standard uncertainty around 1%) both in terms of detection efficiency indicator (T/D) and count rate (D). Thus, we demonstrate a remarkable reproducibility, which means that Hf-DPA captures the ^{85}Kr but also releases it when rinsing with air. No memory effect is visible during the measurements (contrary to what we observed in some plastics scintillators), making this type of MOF of great interest for the development of detection instrumentation.

Table 9. Reproducibility measurement on a same Hf-MOF sample with similar activity concentration. Standard uncertainties of the results are in parenthesis.

Total Activity of ^{85}Kr in the circuit, A (kBq)	CW 40 ns		CW 400 ns	
	D/A (s^{-1}/Bq)	T/D	D/A (s^{-1}/Bq)	T/D
10.65 (9)	0.01437 (18)	0.296 (7)	0.0203 (5)	0.257 (10)
10.43 (8)	0.01441 (9)	0.3043 (38)	0.02008 (16)	0.2658 (30)
10.37 (8)	0.01451 (13)	0.3027 (46)	0.02020 (15)	0.2639 (30)

13. SUPPLEMENTARY REFERENCES

- 1 Mallick, A. *et al.* Unprecedented ultralow detection limit of amines using a thiadiazole-functionalized Zr (IV)-based metal–organic framework. *Journal of the American Chemical Society* **141**, 7245-7249 (2019).
- 2 Gosselin, A. J. *et al.* Ligand-based phase control in porous zirconium coordination cages. *Chemistry of Materials* **32**, 5872-5878 (2020).
- 3 Vogt, J. r. & Alvarez, S. van der Waals radii of noble gases. *Inorganic chemistry* **53**, 9260-9266 (2014).
- 4 METz, G., Wu, X. & Smith, S. O. Ramped-amplitude cross polarization in magic-angle-spinning NMR. *Journal of Magnetic Resonance, Series A* **110**, 219-227 (1994).
- 5 Vinogradov, E., Madhu, P. K. & Vega, S. High-resolution proton solid-state NMR spectroscopy by phase-modulated Lee–Goldburg experiment. *Chemical Physics Letters* **314**, 443-450 (1999).
- 6 Leskes, M., Madhu, P. K. & Vega, S. A broad-banded z-rotation windowed phase-modulated Lee–Goldburg pulse sequence for ^1H spectroscopy in solid-state NMR. *Chemical Physics Letters* **447**, 370-374 (2007).
- 7 Bennett, A. E., Rienstra, C. M., Auger, M., Lakshmi, K. & Griffin, R. G. Heteronuclear decoupling in rotating solids. *The Journal of chemical physics* **103**, 6951-6958 (1995).
- 8 Perego, J. *et al.* Composite fast scintillators based on high-Z fluorescent metal–organic framework nanocrystals. *Nature Photonics* **15**, 393-400 (2021).
- 9 Coelho, A. & Kern, A. Discussion of the indexing algorithms within TOPAS. *CPD Newsletter* **32**, 43-45 (2005).
- 10 Inc., A. S. Materials Studio Modeling Environment. *Release 5.0*, San Diego: (2007).
- 11 Schneider, C. A., Rasband, W. S. & Eliceiri, K. W. NIH Image to ImageJ: 25 years of image analysis. *Nature methods* **9**, 671-675 (2012).
- 12 Morris, J. V., Mahaney, M. A. & Huber, J. R. Fluorescence quantum yield determinations. 9,10-Diphenylanthracene as a reference standard in different solvents. *The Journal of Physical Chemistry* **80**, 969-974, doi:10.1021/j100550a010 (1976).

- 13 Kubin, R. F. & Fletcher, A. N. Fluorescence quantum yields of some rhodamine dyes. *Journal of Luminescence* **27**, 455-462 (1982).
- 14 Broda, R., Cassette, P. & Kossert, K. Radionuclide metrology using liquid scintillation counting. *Metrologia* **44**, S36 (2007).
- 15 Sabot, B., Dutsov, C., Cassette, P. & Mitev, K. Performance of portable TDCR systems developed at LNE-LNHB. *Nuclear Instruments and Methods in Physics Research Section A: Accelerators, Spectrometers, Detectors and Associated Equipment* **1034**, 166721 (2022).
- 16 Jordanov, V., Cassette, P., Dutsov, C. & Mitev, K. Development and applications of a miniature TDCR acquisition system for in-situ radionuclide metrology. *Nuclear Instruments and Methods in Physics Research Section A: Accelerators, Spectrometers, Detectors and Associated Equipment* **954**, 161202 (2020).
- 17 Birks, J. B. *The theory and practice of scintillation counting: International series of monographs in electronics and instrumentation*. Vol. 27 (Elsevier, 2013).